Molecular Cell

Article

Effector-mediated membrane disruption controls cell death in CBASS antiphage defense

Graphical abstract

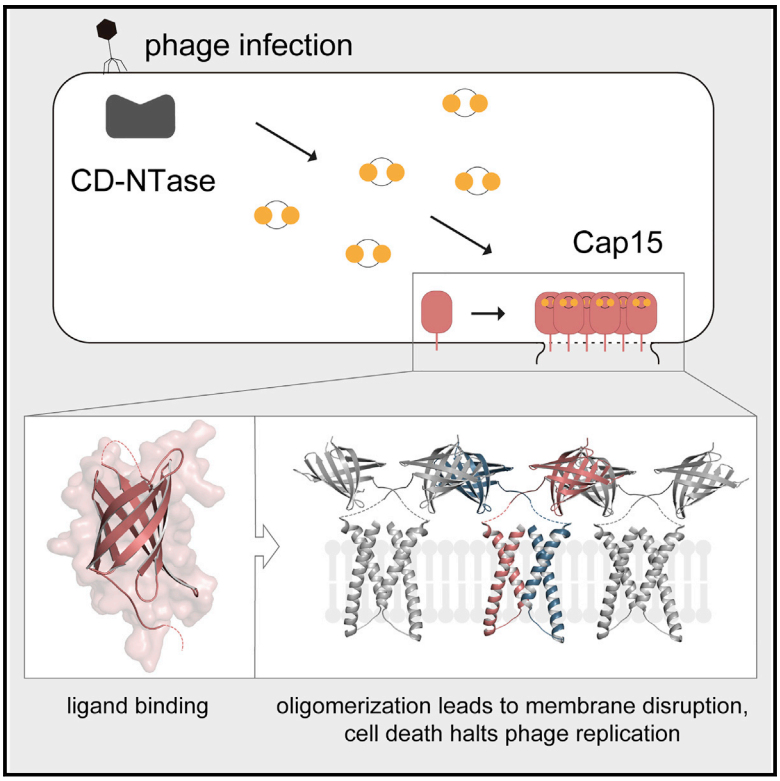

Authors

Brianna Duncan-Lowey,
Nora K. McNamara-Bordewick,
Nitzan Tal, Rotem Sorek,
Philip J. Kranzusch

Correspondence

philip_kranzusch@dfci.harvard.edu

In brief

Duncan-Lowey et al. determine the function of transmembrane effectors in CBASS antiphage defense. Transmembrane effectors bind nucleotide second messengers, induce inner-membrane disruption, and cause cell death to limit phage replication. The structure of one family of transmembrane effectors, Cap15, reveals a minimal β-barrel that binds activating cyclic dinucleotide signals.

Highlights

- CBASS antiphage transmembrane effectors induce membrane disruption and cell death
- The TM effector Cap15 contains a β-barrel domain for second messenger recognition
- Ligand binding triggers Cap15 oligomerization and inner-membrane disruption
- Cap15 effectors disrupt membranes through raft-like clustering, not pore formation

Duncan-Lowey et al., 2021, Molecular Cell *81*, 1–13
December 16, 2021
https://doi.org/10.1016/j.molcel.2021.10.020

CellPress

Please cite this article in press as: Duncan-Lowey et al., Effector-mediated membrane disruption controls cell death in CBASS antiphage defense, Molecular Cell (2021), https://doi.org/10.1016/j.molcel.2021.10.020

Molecular Cell

CellPress

Article

Effector-mediated membrane disruption controls cell death in CBASS antiphage defense

Brianna Duncan-Lowey,[1,2] Nora K. McNamara-Bordewick,[2] Nitzan Tal,[3] Rotem Sorek,[3] and Philip J. Kranzusch[1,2,4,5,*]
[1]Department of Microbiology, Harvard Medical School, Boston, MA 02115, USA
[2]Department of Cancer Immunology and Virology, Dana-Farber Cancer Institute, Boston, MA 02115, USA
[3]Department of Molecular Genetics, Weizmann Institute of Science, Rehovot, Israel
[4]Parker Institute for Cancer Immunotherapy at Dana-Farber Cancer Institute, Boston, MA 02115, USA
[5]Lead contact
*Correspondence: philip_kranzusch@dfci.harvard.edu
https://doi.org/10.1016/j.molcel.2021.10.020

SUMMARY

Cyclic oligonucleotide-based antiphage signaling systems (CBASS) are antiviral defense operons that protect bacteria from phage replication. Here, we discover a widespread class of CBASS transmembrane (TM) effector proteins that respond to antiviral nucleotide signals and limit phage propagation through direct membrane disruption. Crystal structures of the *Yersinia* TM effector Cap15 reveal a compact 8-stranded β-barrel scaffold that forms a cyclic dinucleotide receptor domain that oligomerizes upon activation. We demonstrate that activated Cap15 relocalizes throughout the cell and specifically induces rupture of the inner membrane. Screening for active effectors, we identify the function of distinct families of CBASS TM effectors and demonstrate that cell death via disruption of inner-membrane integrity is a common mechanism of defense. Our results reveal the function of the most prominent class of effector protein in CBASS immunity and define disruption of the inner membrane as a widespread strategy of abortive infection in bacterial phage defense.

INTRODUCTION

In bacteria, cyclic oligonucleotide-based antiphage signaling systems (CBASS) are a major form of antiviral defense that limit replication of diverse phages (Cohen et al., 2019). Each CBASS operon contains a cGAS/DncV-like nucleotidyltransferase (CD-NTase) enzyme that functions to sense phage replication and a partner CD-NTase-associated protein (Cap) effector that directly impairs host cell function to prevent viral spread (Lowey et al., 2020; Whiteley et al., 2019; Ye et al., 2020). Following recognition of phage infection, the CD-NTase synthesizes a nucleotide second messenger, which then directly binds the Cap effector and results in activation and induction of antiviral defense (Cohen et al., 2019; Lau et al., 2020; Lowey et al., 2020; Whiteley et al., 2019).

A critical step in CBASS immunity is the ability of the Cap effector to respond to a specific CD-NTase nucleotide second messenger signal (Govande et al., 2021; Lowey et al., 2020). Bacterial CD-NTase enzymes produce a diverse array of nucleotide signals with distinct base and phosphodiester linkage specificity, including cyclic dinucleotide (e.g., 3′3′ cyclic GMP-AMP, 3′3′-cGAMP) and cyclic trinucleotide (e.g., 3′3′ cyclic AMP-AMP-GMP, 3′3′3′-cAAG) products (Lowey et al., 2020; Whiteley et al., 2019). Recent structures of CBASS effectors in complex with nucleotide second messengers explain how correct signal recognition controls protein function (Lau et al., 2020; Lowey et al., 2020; Morehouse et al., 2020). The structure of *A. baumannii* Cap4 demonstrates that a protein domain named SAVED is responsible for nucleotide recognition and subsequent protein oligomerization to control effector activation (Lowey et al., 2020). Interestingly, the Cap4 SAVED domain is a structural homolog of CRISPR-associated Rossman fold (CARF)-family proteins, revealing structural and functional overlap between components of CBASS and CRISPR immune systems (Jia et al., 2019; Lowey et al., 2020; Niewoehner and Jinek, 2016). Likewise, discovery of a bacterial domain homologous to the human cyclic dinucleotide binding protein stimulator of interferon genes (STING) within CBASS effectors Cap12 and Cap13 demonstrates an evolutionary link between CBASS nucleotide-second messenger binding and components of animal innate immunity (Morehouse et al., 2020). These CBASS effectors containing STING and SAVED domains specifically bind nucleotide second messengers, then oligomerize when activated. The majority of CBASS operons, however, contain effectors with no characterized nucleotide-binding domain, suggesting that major forms of nucleotide second messenger recognition remain to be discovered.

Following nucleotide second messenger recognition, Cap effectors induce cell death to kill the host bacteria and block phage replication through a form of antiviral defense termed abortive infection. Nearly all characterized abortive infection defense systems function through effectors with enzymatic domains that degrade or modify target host or phage proteins (Lopatina et al., 2020). Several CBASS enzymatic effectors downstream

Please cite this article in press as: Duncan-Lowey et al., Effector-mediated membrane disruption controls cell death in CBASS antiphage defense, Molecular Cell (2021), https://doi.org/10.1016/j.molcel.2021.10.020

of CD-NTases have been mechanistically characterized, including phospholipases (CapV), DNA endonucleases (Cap4, Cap5, NucC), and NADases (Cap12) (Cohen et al., 2019; Lau et al., 2020; Lowey et al., 2020; Morehouse et al., 2020; Severin et al., 2018). The nuclease effectors Cap4, Cap5, and NucC indiscriminately degrade double-stranded DNA (dsDNA) upon activation (Lau et al., 2020; Lowey et al., 2020), while the phospholipase effector CapV cleaves membrane phospholipids leading to cell death (Cohen et al., 2019; Severin et al., 2018). However, the majority of CBASS operons do not contain enzymatic effectors and instead encode uncharacterized proteins with predicted transmembrane (TM) segments (Burroughs et al., 2015; Millman et al., 2020). While it has been hypothesized that these effectors lead to membrane disruption, it is unknown how TM effectors function to restrict phage replication.

Here, we discover that CBASS TM effectors are potent antiphage defense proteins that destroy bacterial inner-membrane integrity and induce host cell death. Through development of a screen to identify active TM effectors, we define the family of CBASS proteins named Cap15 that respond to cyclic dinucleotide signals and block phage replication. High-resolution crystal structures of the Cap15 nucleotide binding domain reveal a compact β-barrel scaffold with a central pocket for ligand recognition and oligomerization interfaces essential for phage defense. Mechanistically, we show that Cap15 oligomerization and activation disrupt bacterial cell integrity and lead to specific disruption of the inner membrane. We further demonstrate that inner-membrane disruption is a widespread mechanism shared between diverse families of CBASS TM effectors that are encoded in both gram-negative and gram-positive bacteria. Our results demonstrate the function of a major class of CBASS effectors controlling antiviral defense and define the host membrane as a common target of bacterial abortive infection defense systems.

RESULTS

Discovery of CBASS TM effectors that terminate cell growth

Building upon previous bioinformatic analysis (Burroughs et al., 2015; Cohen et al., 2019; Millman et al., 2020; Whiteley et al., 2019), we analyzed putative effector proteins in CBASS operons and identified a diverse set of 2,234 proteins containing TM segments. TM effectors are encoded in >40% of CBASS operons, representing a dominant form of effector that occurs more frequently than previously characterized phosphodiesterase, nuclease, or NADase proteins with enzymatic function (Figure 1A) (Lau et al., 2020; Lowey et al., 2020; Morehouse et al., 2020; Severin et al., 2018). The most common TM effector contains two TM segments fused to an uncharacterized β-strand-rich C-terminal domain, and we named this effector CD-NTase-associated protein 15 (Cap15) (Figures 1B and 1C). To determine if Cap15 is capable of responding to CBASS cyclic dinucleotide signaling and inducing cell toxicity in bacteria, we leveraged the known ability of the CD-NTase *Vibrio cholerae* DncV (*Vc*DncV; NCBI ref. WP_001901330.1) to be auto-activated as a promiscuous 3′3′-cGAMP synthase during overexpression in *E. coli* (Whiteley et al., 2019; Zhou et al., 2018). *Vc*CapV is a phospholipase known to be activated by 3′3′-cGAMP in CBASS defense and robustly induces toxicity in these conditions (Cohen et al., 2019; Severin et al., 2018) (Figure 1D). Expression of *Escherichia albertii* Cap15 (*Ea*Cap15, NCBI ref. WP_206748793.1) in the presence of active 3′3′-cGAMP signaling prevents culture growth (Figure 1D) and induces cell death as confirmed by flow cytometry (Figure S1D). A *Vc*DncV D131A, D133A substitution that disrupts CD-NTase catalytic function rescues cell viability, demonstrating that *Ea*Cap15 induces cell death only in the presence of active 3′3′-cGAMP nucleotide second messenger signaling (Figure 1D).

We next screened a panel of 23 CBASS TM effectors and identified a wide diversity of proteins capable of inducing cell toxicity specifically in response to 3′3′-cGAMP (Figure 1E). Toxic TM effector proteins belong to several families including Cap14 proteins (TM-SAVED, Pfam PF18145) and Cap16 proteins (TM-NUDIX, Pfam PF18167) (Figures 1E and S1A). TM effectors are encoded throughout the CD-NTase family tree (Whiteley et al., 2019), suggesting that the effectors not responsive to 3′3′-cGAMP in our screen likely induce cell death but respond to other CD-NTase products including pyrimidine-containing cyclic dinucleotide and cyclic trinucleotide signals (Lowey et al., 2020; Whiteley et al., 2019). In each case, cell toxicity is strictly dependent on the presence of TM segments, revealing that membrane association is essential for TM effector function (Figures 1F and S1B). The only TM effector with a putative enzymatic domain is Cap16, which contains a NUDIX hydrolase domain (Figures 1B and 1C). Mutation of the putative Cap16 active site (E154A) does not impact cell toxicity (Figures 1F and S1B), further confirming that TM effector function is dependent on TM segments and not catalytic activity. These data define Cap15 and diverse TM effectors in CBASS immunity that respond to antiviral nucleotide second messenger signaling and induce potent cell toxicity.

CBASS Cap15 TM effectors protect bacteria from phage infection and encode a minimal β-barrel domain

To determine the role of TM effectors in antiviral defense, we expressed complete Cap15-containing CBASS operons in *E. coli* and challenged the bacteria with a panel of 10 diverse phages. CBASS operons containing Cap15 effectors potently restrict viral plaque formation (Figures 2A and 2B). The *Escherichia* CBASS (*Ea*CdnB [NCBI ref. WP_000995828.1] and *Ea*Cap15 [NCBI ref. WP_206748793.1]), which we identified as a 3′3′-cGAMP signaling system (Figure 1D), protects *E. coli* against infection with T2, T5, and T6 (Figure 2A). Interestingly, a related *Yersinia* CBASS operon, which encodes homologous CD-NTase and Cap15 components (*Ya*CdnE [NCBI ref. WP_145567548.1] and *Ya*Cap15 [NCBI ref. WP_145567547.1]), protects *E. coli* against all tested *Myoviridae* (T2, T4, T6), *Siphoviridae* (T5, SECphi4, SECphi6, SECphi18, SECphi27), and the single-stranded DNA (ssDNA) phage SECphi17, but not the *Podoviridae* phage T7, demonstrating a variable range of phage defense between CBASS operons encoding the same class of effector (Figure 2B). We analyzed CBASS Cap15-containing operons and observed that they are widely distributed in both gram-negative and gram-positive bacteria (Figure 2C). CBASS Cap15-containing operons protect against a wide diversity of phages, including

Please cite this article in press as: Duncan-Lowey et al., Effector-mediated membrane disruption controls cell death in CBASS antiphage defense, Molecular Cell (2021), https://doi.org/10.1016/j.molcel.2021.10.020

CellPress

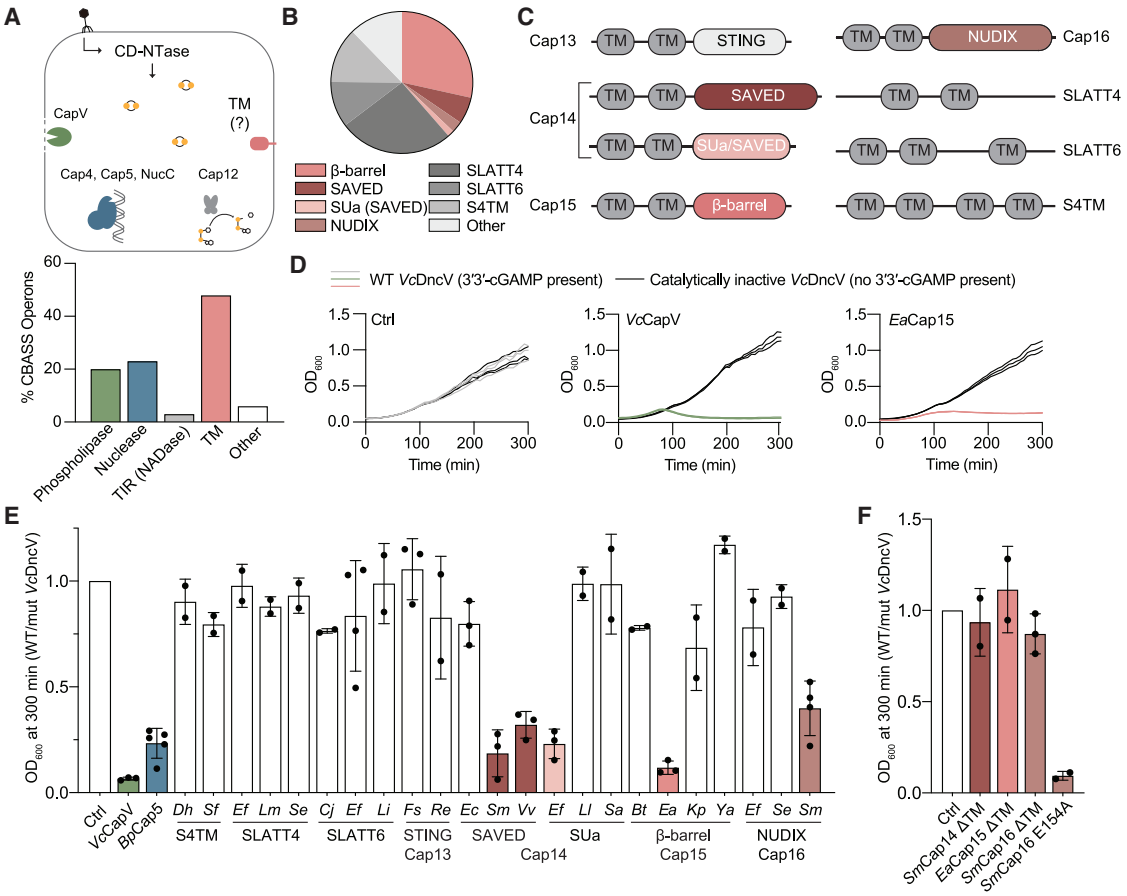

Figure 1. Discovery of CBASS TM effectors that control cell death

(A) Schematic showing CBASS effector types and abundance in sequenced genomes. Transmembrane (TM) effectors are encoded in >40% of CBASS operons.

(B) Quantification of individual families of TM effectors in CBASS operons.

(C) Domain organization of common CBASS TM effector families. Structure prediction analysis demonstrates that SUa (Pfam PF18179) is a variant of the SAVED nucleotide-binding domain. See also Figure S1.

(D) Growth curves of *E. coli* expressing a CBASS effector protein and the 3′3′-cGAMP synthase *Vibrio cholerae* DncV (*Vc*DncV). *Vc*DncV is known to catalyze active 3′3′-cGAMP signaling upon overexpression in *E. coli* (Whiteley et al., 2019; Zhou et al., 2018). Cells expressing WT *Vc*DncV are indicated in color, and catalytically inactive *Vc*DncV are in gray. The 3′3′-cGAMP-responsive effectors induce cell death upon co-expression with active *Vc*DncV.

(E) Quantification of growth curves and cell death induced by 3′3′-cGAMP-responsive effector proteins. Data are displayed as the difference in OD_{600} of cultures expressing WT versus catalytically inactive *Vc*DncV 300 min after induction, relative to a control culture with no effector expression. Many families of TM-containing effectors cause cell death in response to 3′3′-cGAMP production.

(F) Quantification of cell death induced by full-length or truncated (ΔTM) TM effectors where the TM domain was replaced by SUMO to ensure solubility. Cap16 contains a putative NUDIX hydrolase domain and was additionally tested with a NUDIX-inactivating E154A mutation. TM-containing effectors require the appended TM segments to induce cell death. Toxicity data are representative of at least two independent experiments. Error bars represent standard deviation (SD). See also Figure S1.

both dsDNA and ssDNA phage, suggesting the viral signal that activates these CBASS operons is broadly conserved. In each case, disruption of the CD-NTase active site or deletion of the Cap15 TM region abolished all phage protection, demonstrating that Cap15-mediated antiviral defense is strictly dependent upon functional CD-NTase signaling and interaction with the bacterial membrane (Figures S2B and S2C).

Each Cap15 protein comprises N-terminal TM helices fused to an uncharacterized C-terminal domain (Figure 1C). To define the molecular basis of Cap15 effector function, we determined a 1.9-Å crystal structure of the *Ya*Cap15 C-terminal domain (Figure 2D; Table 1). The *Ya*Cap15 structure reveals eight β strands (β2–β9) that wrap and form a compact β-barrel (Figure 2D). Strikingly, the closest structural homologs to Cap15 are not natural proteins, but instead are computationally derived β-barrel proteins designed to bind fluorescent small molecules (Figure 2E) (Dou et al., 2018). Similar to the rationally designed proteins, in Cap15, a set of nine glycine residues distributed throughout the eight β strands are positioned to increase strand curvature, reduce side chain density within the barrel center, and enable folding of the minimized β-barrel structure (Figures S2D and S2E). Cap15 is further stabilized by a conserved "tryptophan corner" interaction previously observed in other β-barrel structures (Dou et al., 2018). In *Ya*Cap15, this interaction occurs where W96 on the

Please cite this article in press as: Duncan-Lowey et al., Effector-mediated membrane disruption controls cell death in CBASS antiphage defense, Molecular Cell (2021), https://doi.org/10.1016/j.molcel.2021.10.020

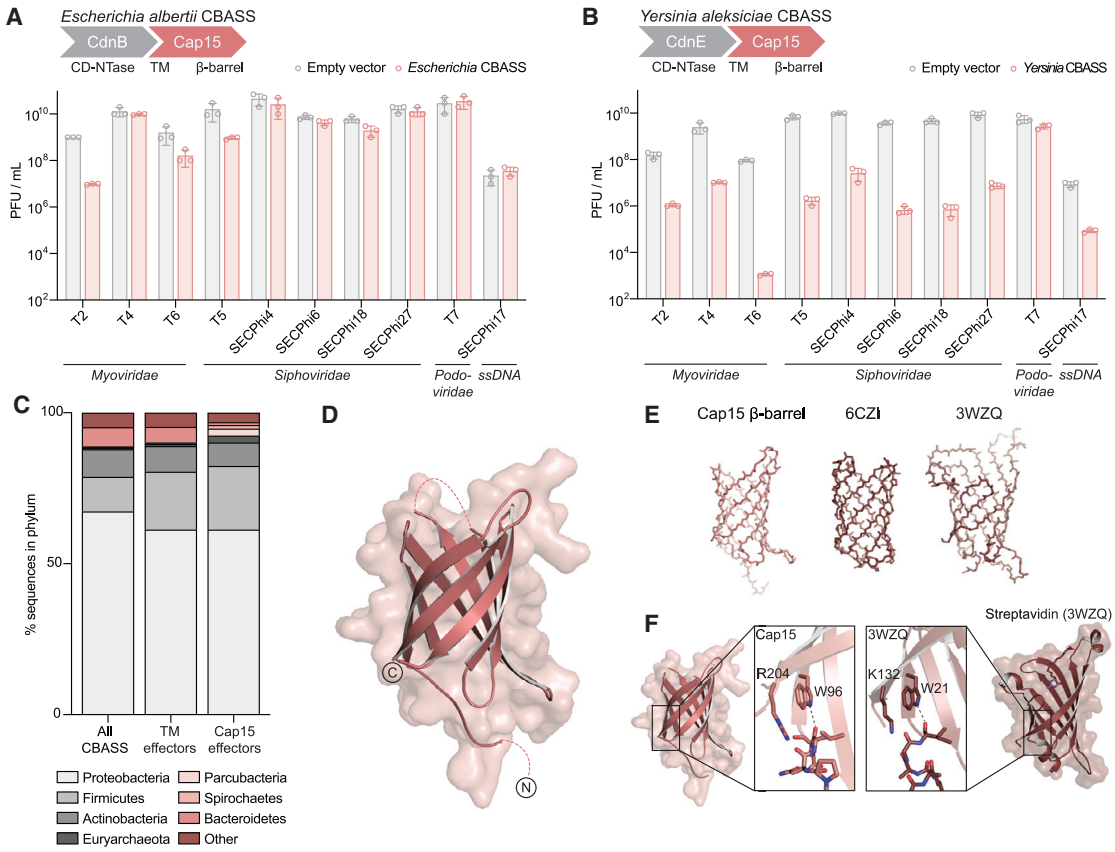

Figure 2. Cap15 protects bacteria from phage infection and encodes a minimal β-barrel nucleotide-binding domain

(A and B) Phage challenge of *E. coli* expressing *Escherichia* or *Yersinia* CBASS operons. CBASS operons containing Cap15 β-barrel TM effectors protect against infection with diverse phages. Cartoon schematic shows organization of the CBASS operons encoding CD-NTases from clade B (CdnB) or E (CdnE) and the Cap15 β-barrel-containing TM effector.

(C) Phylogenetic analysis of the distribution of Cap15 β-barrel effectors and other CBASS TM effectors across bacterial phyla demonstrates widespread occurrence in both gram-negative and gram-positive bacteria.

(D) Crystal structure of the *Yersinia aleksiciae* Cap15 (*Ya*Cap15) β-barrel nucleotide-binding domain. The *Ya*Cap15 structure consists of eight β strands that form a highly minimized β-barrel.

(E) Comparison of Cap15 to an *in-silico*-designed small-molecule sensor (6CZI) (Dou et al., 2018) and the biotin-binding protein streptavidin (3WZQ) (Kawato et al., 2015).

(F) The Cap15 β-barrel domain contains a common tryptophan-corner capping motif at the bottom of the β-barrel similar to streptavidin proteins. A capping helix common to many β-barrels is replaced by a capping β strand in Cap15.

Phage defense data are representative of at least three independent experiments. Error bars represent SD. See also Figure S2.

N-terminal strand β2 stacks against R204 on the C-terminal strand β9 and forms a hydrogen bond with the peptide carboxyl on strand β1 below the β-barrel (Figure 2F). Together, these data define the TM effector Cap15 as a widespread β-barrel domain-containing protein that enables CBASS antiphage defense.

Cap15 β-barrel nucleotide-binding domain specifically binds uracil-containing cyclic dinucleotides

The Cap15 β-barrel domain creates a solvent-exposed pocket at the top of the protein that is in the same location as the small-molecule binding site of rationally designed β-barrels (Figure 3A) (Dou et al., 2018). Additionally, Cap15 exhibits more distantly related structural homology to streptavidin proteins that form a similar pocket at the top of a β-barrel domain to create a binding site for biotin (Figure S3A). Therefore, we hypothesized that the function of the Cap15 β-barrel domain is to recognize the CD-NTase product nucleotide second messenger. To test this hypothesis, we purified the *Yersinia aleksiciae* CD-NTase (*Ya*CdnE) encoded adjacent to *Ya*Cap15 and determined the nucleotide second messenger product for this CBASS operon using ^{32}P-labeled nucleotides and thin-layer chromatography. *Ya*CdnE synthesizes a mixture of di-pyrimidine and purine-pyrimidine cyclic dinucleotide products with a strong preference for incorporation of UTP (Figure 3B). HPLC (Figures 3C and S3B) and mass spectrometry analysis of the purified reaction products demonstrate that the most abundant products synthesized by *Ya*CdnE in the presence of ATP, GTP, CTP, and UTP are 3′3′-c-di-UMP (*m/z* = 613.058) and 3′3′-cUMP-AMP (*m/z* = 636.085).

We next analyzed the ability of the *Ya*Cap15 C-terminal β-barrel domain to bind radiolabeled *Ya*CdnE cyclic

Please cite this article in press as: Duncan-Lowey et al., Effector-mediated membrane disruption controls cell death in CBASS antiphage defense, Molecular Cell (2021), https://doi.org/10.1016/j.molcel.2021.10.020

Table 1. Crystallographic statistics

	*Ya*Cap15 (SeMet phasing)	*Ya*Cap15 (SeMet refinement)	*Ya*Cap15
Data collection			
Resolution (Å)[a]	37.09–2.30 (2.38–2.30)	37.01–1.90 (1.94–1.90)	44.05–2.60 (2.72–2.60)
Wavelength (Å)	0.97918	0.97918	0.97918
Space group	C 1 2 1	C 1 2 1	P 6_1
Unit cell: a, b, c (Å)	93.51, 31.20, 50.04	93.29, 31.04, 50.02	50.87, 50.87, 155.02
Unit cell: α, β, γ (°)	90.0, 100.33, 90.0	90.0, 100.22, 90.0	90.0, 90.0, 120.0
Molecules per ASU	1	1	2
Total reflections	487276	77567	111881
Unique reflections	6554	11344	7040
Completeness (%)[a]	99.8 (98.1)	99.8 (98.9)	100.0 (100.0)
Multiplicity[a]	74.3 (71.4)	6.9 (6.3)	15.9 (15.2)
$I/\sigma I$[a]	25.8 (6.1)	13.3 (1.3)	19.3 (1.3)
CC(1/2)[b] (%)[a]	99.9 (43.2)	99.9 (56.2)	100.0 (51.2)
Rpim[c] (%)[a]	2.7 (75.0)	2.9 (64.3)	1.8 (67.4)
Sites	1		
Refinement			
Resolution (Å)		37.0–1.90	44.05–2.60
Free reflections		1134	679
R-factor/R-free		21.5 / 25.4	29.7 / 31.3
Bond distance (RMS Å)		0.006	0.002
Bond angles (RMS °)		0.752	0.491
Structure/stereochemistry			
No. atoms: protein		869	1687
No. atoms: solvent		24	0
Average B-factor: protein		54.89	108.24
Average B-factor: water		54.08	N/A
Ramachandran plot: favored		99.02%	95.41%
Ramachandran plot: allowed		0.98%	4.59%
Ramachandran plot: outliers		0.00%	0.00%
Rotamer outliers		1.11%	4.55%
MolProbity[d] score		1.12	2.20
Protein Data Bank ID		7N34	7N35

[a]Highest-resolution shell values in parentheses.
[b]Karplus and Diederichs (2012)
[c]Weiss (2001)
[d]Chen et al. (2010)

dinucleotide products and observed specific recognition of 3′3′-c-di-UMP and 3′3′-cUMP-AMP (Figures 3D, 3E, S3C, and S3D). *Ya*Cap15 binds 3′3′-c-di-UMP and 3′3′-cUMP-AMP with ~100-nM affinity and exhibits no ability to interact with the control cyclic dinucleotide 3′3′-c-di-AMP (Figures 3D, 3E, and S3C–S3E). Additionally, we observed that Cap15 binding to any UMP-containing cyclic dinucleotide results in a dramatic increase in the thermostability of the complex, further supporting a direct role for the Cap15 C-terminal β-barrel domain in sensing the CD-NTase cyclic dinucleotide antiviral signal (Figures 3F and S3F).

Analysis of the Cap15 solvent exposed pocket at the top of the β-barrel reveals highly conserved residues surrounding the putative nucleotide-binding site (Figures 3G, 3H, and S2A). To confirm the role of this Cap15 pocket in mediating cyclic dinucleotide recognition, we next mutated each conserved residue to eliminate potential hydrogen-bonding interactions (Y153F, Y155F, Y188F, M200I) or inserted bulkier side chains to limit access to the binding site (T129Q, N157Q). Substitutions to the conserved *Ya*Cap15 pocket residues each reduce 3′3′-c-di-UMP binding or abrogate all ligand recognition *in vitro* (Figures 3I and S3G). We confirmed that all mutations, with the

Please cite this article in press as: Duncan-Lowey et al., Effector-mediated membrane disruption controls cell death in CBASS antiphage defense, Molecular Cell (2021), https://doi.org/10.1016/j.molcel.2021.10.020

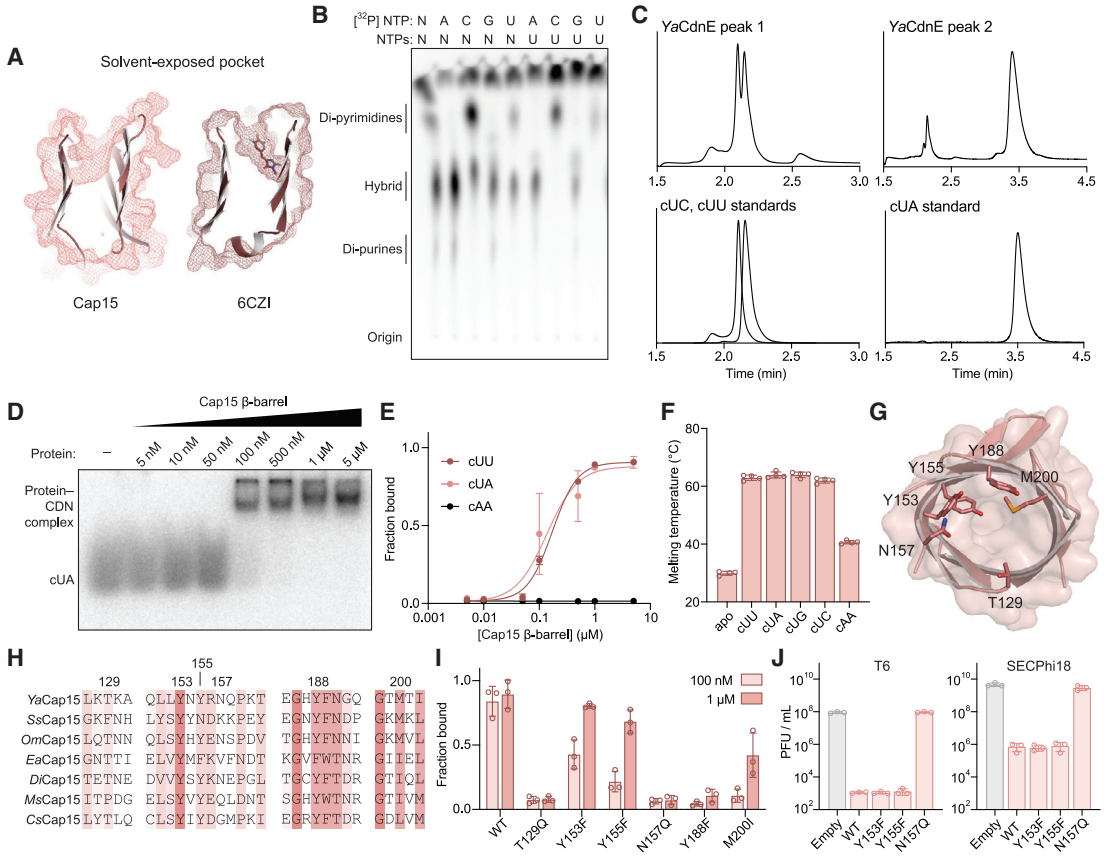

Figure 3. Cap15 β-barrel nucleotide-binding domain specifically binds uracil-containing cyclic dinucleotides

(A) Cutaway slice through the center of Cap15 (left) and the rationally designed small-molecule sensor 6CZI (right). Protein surface is represented in mesh, and the small molecule bound to 6CZI is shown in sticks. A solid, hydrophobic core stabilizes the bottom of each β-barrel creating a solvent-exposed pocket at the top lined with hydrophilic amino acids for ligand recognition.

(B) Analysis of *Ya*CdnE nucleotide second messenger synthesis. *Ya*CdnE was incubated with α-^{32}P-NTPs, and reactions were phosphatase treated and separated by thin-layer chromatography.

(C) HPLC analysis of *Ya*CdnE products after separation by ion exchange chromatography. *Ya*CdnE products were separated as two major peaks from ion exchange and were analyzed separately by HPLC (top) compared to cyclic dinucleotide standards (bottom). *Ya*CdnE synthesizes 3′3′-c-di-UMP, 3′3′-cUMP-AMP, and 3′3′-cUMP-CMP as major products. See also Figure S3B.

(D) Electrophoretic mobility shift assay measurement of *Ya*Cap15-3′3′-cUMP-AMP complex formation. A titration of *Ya*Cap15 (5 nM–5 μM) was incubated with 10-nM ^{32}P-labeled 3′3′-cUMP-AMP, and bound complexes were resolved by nondenaturing polyacrylamide gel electrophoresis.

(E) Quantification of *Ya*Cap15-cyclic dinucleotide complex formation as shown in (D). See also Figures S3C and S3E.

(F) Thermal denaturation assay to quantify stabilization of the *Ya*Cap15 β-barrel upon binding to UMP-containing cyclic dinucleotides. Cyclic dinucleotide recognition leads to an ~25°C increase in *Ya*Cap15 β-barrel melting temperature, demonstrating significant stabilization.

(G) Cartoon highlighting conserved residues lining the Cap15 β-barrel solvent-exposed nucleotide-binding pocket.

(H) Conservation of select residues lining the Cap15 nucleotide-binding pocket. *Ya*Cap15 binds UMP-containing cyclic dinucleotides; *Ea*Cap15 is activated by 3′3′-cGAMP.

(I) Quantification of 3′3′-c-di-UMP binding assays using *Ya*Cap15 proteins with point mutations within the nucleotide-binding pocket verifies the importance of individual contacts for nucleotide second messenger recognition. *Ya*Cap15 mutants were incubated at 100-nM or 1-μM concentration with 3′3′-c-di-UMP, and complex formation was quantified as in (E). See also Figure S3G.

(J) Phage challenge of *E. coli* expressing *Yersinia* CBASS with mutations to the Cap15 nucleotide-binding pocket (empty vector controls shown in Figure 2B are included again for reference). Mutations that inhibit nucleotide binding abolish protection from phage infection.

Biochemical and phage defense data are representative of at least three independent experiments. Error bars represent SD. See also Figure S3.

exception of M200I, did not negatively impact protein stability (Figure S3H). We next determined whether mutations that disrupt Cap15 ligand binding prevent CBASS antiphage defense. We observed that a *Ya*Cap15 N157Q mutation predicted to occlude the nucleotide-binding pocket results in complete loss of phage protection, while mutations that only mildly decrease ligand binding (Y153F, Y155F) do not affect phage defense (Figures 3J and S3I). Together, these results demonstrate the discovery of a class of minimal β-barrel cyclic dinucleotide binding domains and reveal the mechanistic basis of Cap15 cyclic dinucleotide recognition in CBASS defense.

Please cite this article in press as: Duncan-Lowey et al., Effector-mediated membrane disruption controls cell death in CBASS antiphage defense, Molecular Cell (2021), https://doi.org/10.1016/j.molcel.2021.10.020

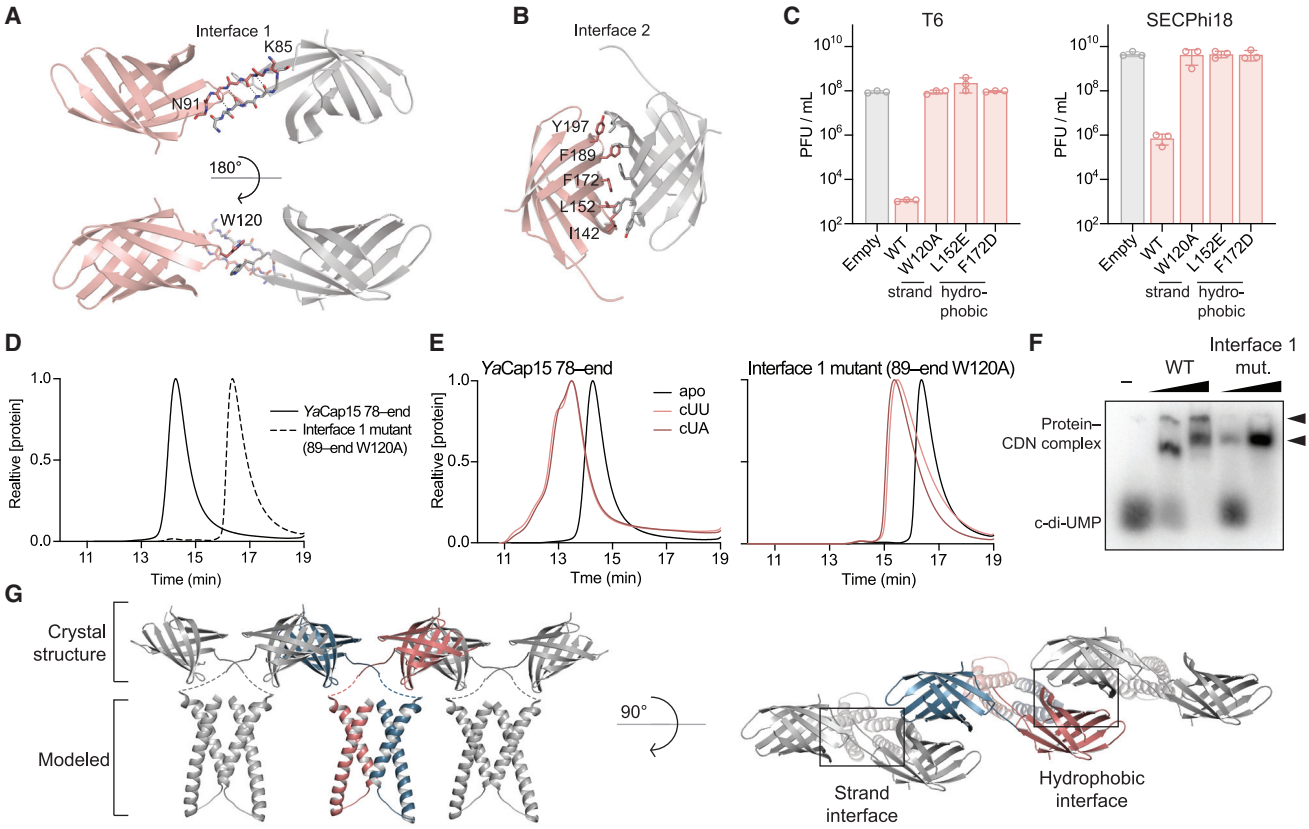

Figure 4. Cap15 oligomerizes upon ligand binding

(A and B) Analysis of packing with symmetry mates in the Cap15 crystal structure defines a β-strand oligomerization interface (interface 1) and a hydrophobic packing interface (interface 2).

(C) Phage challenge of *E. coli* expressing *Yersinia* CBASS with mutations to the oligomerization interfaces (empty vector controls shown in Figure 2B are included again for reference).

(D) SEC demonstrating oligomerization of WT *Ya*Cap15, which is disrupted by mutations to *Ya*Cap15 interface 1 (89–end, W120A).

(E) SEC demonstrating that recognition of activating cyclic dinucleotides results in *Ya*Cap15 higher-order complex formation (left). Mutations to *Ya*Cap15 interface 1 prevent full higher-order complex formation but do not impact cyclic dinucleotide recognition (right).

(F) Electrophoretic mobility shift assay measurement of WT or interface 1 mutant Cap15 binding to 3′3′-c-di-UMP. 100 nM or 1 μM of indicated protein was incubated with 10 nM ^{32}P-labeled 3′3′-c-di-UMP, and bound complexes were resolved by nondenaturing polyacrylamide gel electrophoresis. Arrows indicate the two complexes formed by Cap15 after ligand binding. The interface 1 mutant disrupts formation of the higher-order *Ya*Cap15 complex (top arrow).

(G) Structural model of Cap15 oligomerization. The experimentally determined structure of the Cap15 β-barrel is shown with modeled TM domains. Both interface 1 and interface 2 are compatible with clustering of Cap15 along a two-dimensional membrane surface.

Biochemical data are representative of at least two independent experiments, and phage defense data are representative of three independent experiments. Error bars represent SD. See also Figure S4.

Cap15 effector function requires protein oligomerization

Following nucleotide second messenger recognition, soluble CBASS effectors including Cap4, Cap12, and NucC are known to activate by oligomerizing into higher-order protein complexes (Lau et al., 2020; Lowey et al., 2020; Morehouse et al., 2020). To determine if protein oligomerization also has a role in activation of CBASS TM effectors, we next examined packing within the *Ya*Cap15 crystal for potential oligomeric interfaces. In the *Ya*Cap15 crystal, strand β1 extends away from the folded domain and forms a tight anti-parallel β-sheet interaction with a partnering strand β1 on the neighboring *Ya*Cap15 protomer (Figure 4A). This interface (interface 1) between neighboring protomers is further stabilized by a stacking interaction between the W120 side chain of each protein (Figure 4A). We identified an additional oligomerization interface (interface 2) between adjacent *Ya*Cap15 protomers mediated by a stripe of hydrophobic residues I142, L152, F172, F189, and Y197 facing out of the barrel (Figures 4B and S2D). We determined a second 2.6-Å structure of *Ya*Cap15 and verified preservation of identical interface 1 and interface 2 contacts within this distinct crystal form (Figure S4A; Table 1). To determine the importance of the observed contacts, we designed mutations that block oligomerization and tested the impact *in vivo* during phage challenge. Mutations that disrupt interface 1 (W120A) or interface 2 (L152E, F172D) completely abolish phage defense (Figures 4C and S4C), demonstrating that the *Ya*Cap15 oligomerization interfaces are essential for effector function.

Please cite this article in press as: Duncan-Lowey et al., Effector-mediated membrane disruption controls cell death in CBASS antiphage defense, Molecular Cell (2021), https://doi.org/10.1016/j.molcel.2021.10.020

We next measured *Ya*Cap15 oligomerization in solution using size-exclusion chromatography with multi-angle light scattering (SEC-MALS). Wild-type (WT) *Ya*Cap15 (15 kDa) migrates as an oligomeric complex with a molecular weight of 91 kDa (Figures 4D and S4D). Interestingly, in the presence of 3′3′-c-di-UMP or 3′3′-cUMP-AMP, the migration profile of *Ya*Cap15 dramatically shifts to a mixture of higher-order species, indicating that CD-NTase signal recognition triggers further protein oligomerization (Figure 4E). *Ya*Cap15 forms a heterogenous population of species after binding to activating cyclic dinucleotides; therefore, it was not possible to define a discrete molecular weight for the higher-order complex.

To determine if *Ya*Cap15 oligomerization is required for nucleotide second messenger recognition, we purified a *Ya*Cap15 β-barrel domain variant where oligomerization interface 1 is disrupted by a W120A mutation and deletion of strand β1 (*Ya*Cap15 89–end W120A, 14 kDa). In contrast to WT *Ya*Cap15, *Ya*Cap15 89–end W120A migrates as a monomer with a calculated molecule weight of 19 kDa (Figures 4D and S4D). In the presence of 3′3′-c-di-UMP or 3′3′-cUMP-AMP, *Ya*Cap15 89–end W120A undergoes a shift to form a dimer (calculated mass of 31 kDa) but fails to form the fully oligomerized assemblies observed with the WT protein (Figures 4E and S4D). Using radiolabeled cyclic dinucleotides, we confirmed that *Ya*Cap15 89–end W120A retains the ability to bind 3′3′-c-di-UMP or 3′3′-cUMP-AMP, demonstrating that full oligomerization is not required for cyclic dinucleotide recognition (Figures 4E and S4B). Similar to previous analysis of Cap12 (Morehouse et al., 2020), we further observed that the *Ya*Cap15 oligomerization-disrupting mutations prevent formation of larger complexes that migrate higher in the gel well during electrophoretic mobility shift assay experiments (Figures 4F and S4B).

Using the experimentally defined *Ya*Cap15 oligomerization interfaces, we constructed a model of full-length *Ya*Cap15 to predict orientation of the N-terminal TM helices (Figure 4G). Notably, the experimentally defined *Ya*Cap15 oligomerization interfaces are compatible with oligomerization along the two-dimensional surface of the bacterial cell membrane. These data support a mechanism where Cap15 exists as a lower-order multimer and subsequently oligomerizes within the membrane after binding to the activating nucleotide second messenger. Together, these results confirm the importance of *Ya*Cap15 oligomerization interfaces *in vivo* and demonstrate that effector oligomerization is feature conserved between divergent CBASS systems with cytosolic or membrane-bound effector proteins.

CBASS TM effectors cause membrane disruption and cell death

Given the requirement of both the Cap15 TM domains and Cap15 protein oligomerization to induce cell death (Figures 1F and 4C), we hypothesized that TM effectors may inhibit phage replication through direct targeting of the cell membrane after activation. To understand how cell death is induced by Cap15 activation, we examined *E. coli* expressing activated *Ea*Cap15 using phase contrast and fluorescence microscopy. Following induction of *Vc*DncV 3′3′-cGAMP signaling, *E. coli* expressing *Ea*Cap15 exhibit a dramatic shrinking of the inner membrane that results in separation from the cell wall and expansion of the periplasmic space (Figure 5A). Activation of *Ea*Cap15 induced no observable defect in the outer membrane (Figure S5A). Bacteria expressing *Ea*Cap15 with catalytically inactive *Vc*DncV, or *Vc*DncV alone, exhibit normal cellular morphology, demonstrating that membrane disruption requires both nucleotide second messenger synthesis and effector activation (Figure 5C). Using a periplasmic-localized mCherry marker (Uehara et al., 2010), we further confirmed that *Ea*Cap15 activation results in clear expansion of the periplasmic space as the disrupted inner membrane pulls away from the cell wall (Figure 5C). Moreover, we observed that activation of the CBASS phospholipase effector *Vibrio cholerae* CapV (*Vc*CapV), which is known to enzymatically degrade the inner membrane (Severin et al., 2018), results in a similar phenotype, supporting a mechanism of membrane collapse due to direct targeting of inner-membrane integrity (Figure 5B).

To better understand the consequence of Cap15 oligomerization and activation, we analyzed Cap15 TM domain sequences in comparison to the TM domains of proteins known to induce membrane disruption. Many classes of membrane-disrupting proteins (e.g., actinoporin, ClyA) are soluble until they are activated, when exposed TM segments then imbed within the membrane and form a pore (Dal Peraro and van der Goot, 2016; Mueller et al., 2009; Tanaka et al., 2015). In each case, the TM regions of these proteins contain a clear hydrophilic face that lines the central channel of the final pore structure (Figures S4E and S4F). In contrast, other membrane-targeting proteins (e.g., phage holin, pinholin) begin poised in the membrane and then cluster into raft-like assemblies to create membrane lesions (Figures S4G and S4H) (Cahill and Young, 2019; Pang et al., 2013; Young et al., 2000). The TM regions of *Ea*Cap15 and CBASS effectors lack hydrophilic faces and more closely match the hydrophobic, uncharged helices that define membrane-disrupting proteins that form raft-like assemblies (Figures S4I and S4J). Further supporting potential mechanistic similarity, activation of phage holin proteins results in a similar phenotype in which collapse of the bacterial inner membrane leads to expansion of the periplasm (Dewey et al., 2010).

To further interrogate this model, we used time-lapse imaging to track Cap15 localization and cell fate throughout each stage of TM effector activation. We labeled *Ea*Cap15 with GFP at the C terminus and confirmed that the fusion protein induces cell death similar to WT Cap15 when co-expressed with active *Vc*DncV (Figure S5B). Consistent with the model of Cap15 beginning poised in the membrane prior to activation, we observed that in the resting state, *Ea*Cap15 localizes to the membrane at the poles of the *E. coli* cell (Figures 5D and S5C). Upon induction of *Vc*DncV expression and onset of 3′3′-cGAMP signaling, *Ea*Cap15 redistributes as puncta throughout the cell membrane and co-localizes with the inner membrane as it collapses away from the cell wall (Figures 5D, 5E, S5C, and S5D). Several minutes after shrinking of the inner membrane, bacteria return to a phase-dark state and become permeable to the live-dead stain TO-PRO-3, indicating cell death (Figures 5F, 5G, and S5E). At this stage, periplasmic mCherry signal leaks throughout the bacterium, confirming rupture of the inner membrane (Figures 5F and 5G). We further confirmed the *Ea*Cap15 TM domains are required to induce the disruption of the membrane (Figure S5F). Finally, we used transmission electron microscopy to examine

Please cite this article in press as: Duncan-Lowey et al., Effector-mediated membrane disruption controls cell death in CBASS antiphage defense, Molecular Cell (2021), https://doi.org/10.1016/j.molcel.2021.10.020

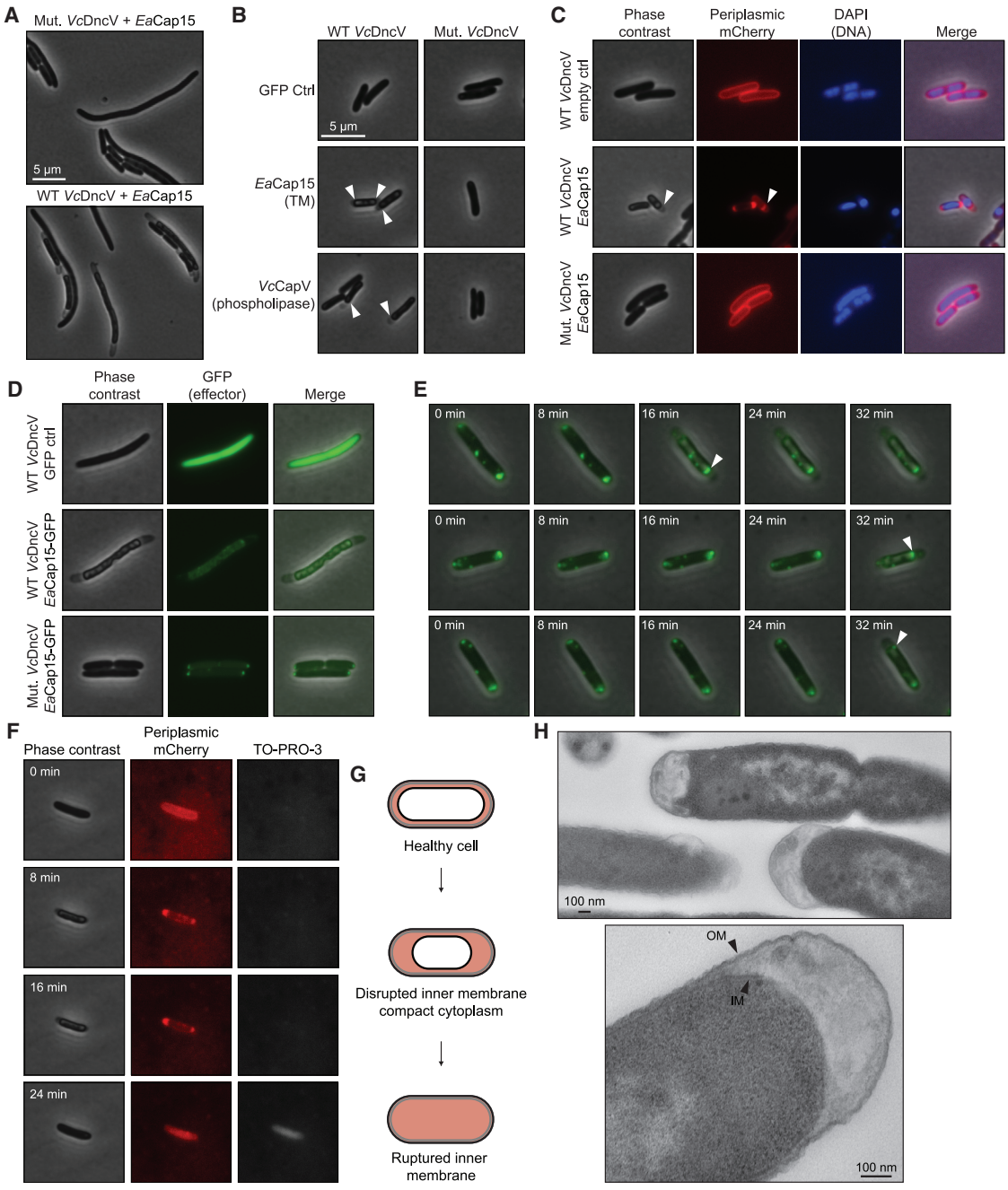

Figure 5. Cap15 activation causes membrane disruption and cell death

(A) Phase contrast image of *E. coli* expressing *Ea*Cap15 effector with WT or catalytically inactive 3′3′-cGAMP synthase *Vc*DncV. Activation of *Ea*Cap15 by 3′3′-cGAMP leads to inner-membrane disruption.

(B) Phase contrast image of *E. coli* expressing GFP control, *Ea*Cap15, or *Vc*CapV effector with WT or catalytically inactive 3′3′-cGAMP synthase *Vc*DncV. Activation of the Cap15 TM effector or CapV phospholipase effector each induce a similar membrane defect (arrows).

(C) Phase contrast and fluorescence microscopy of *E. coli* expressing WT or mutant *Vc*DncV and *Ea*Cap15 or an empty vector control. A periplasmic mCherry marker was co-expressed to allow visualization of expansion of the periplasm (arrows) during Cap15 activation.

(D) *E. coli* expressing GFP or GFP-labeled *Ea*Cap15 with WT or catalytically inactive *Vc*DncV. In the inactive state, *Ea*Cap15-GFP localizes to the poles of the bacterial cell. The 3′3′-cGAMP signaling induces Cap15 activation and redistribution throughout the cell inner membrane.

(E) Time-lapse images of *E. coli* in (C). *Ea*Cap15-GFP redistributes throughout the bacterial cell upon activation and moves with the inner membrane upon collapse (arrows).

(legend continued on next page)

Please cite this article in press as: Duncan-Lowey et al., Effector-mediated membrane disruption controls cell death in CBASS antiphage defense, Molecular Cell (2021), https://doi.org/10.1016/j.molcel.2021.10.020

the membranes of cells dying after Cap15 activation and confirmed that the inner membrane specifically collapses away from the cell wall (Figure 5H).

To expand upon these observations with Cap15, we assessed the structurally distinct CBASS TM effector Cap14 (TM-SAVED). Similar to *Ea*Cap15, activation of *Vibrio vulnificus* Cap14 (*Vv*Cap14; NCBI ref. WP_017790126.1) specifically induces inner-membrane disruption (Figures S5G and S5H). Interestingly, cells expressing each TM effector exhibit distinct morphologies, with *Ea*Cap15 inducing collapse associated with pulling the inner membrane away from the poles of the cell and *Vv*Cap14 separating the cytoplasm into two segments from the center (Figure S5G). After several minutes, *E. coli* expressing active *Vv*Cap14 similarly undergo inner-membrane rupture and cell death, with the release of periplasmic mCherry into the bacterium and the cells becoming permeable to TO-PRO-3 dye (Figures S5H and S5K).

Together, these data demonstrate that CBASS TM effectors limit phage replication by disrupting the bacterial cell membrane and initiating a cell death cascade. The data support a model in which CBASS nucleotide second messenger signaling triggers membrane-bound TM effectors to oligomerize into large assemblies that disrupt the inner membrane and induce cell death (Figure S5L).

DISCUSSION

Our results define bacterial cell membrane disruption as a widespread mechanism controlling abortive infection in CBASS antiphage defense. Following phage infection, CBASS immunity begins with activation of a CD-NTase enzyme to synthesize an antiviral nucleotide second messenger signal. We demonstrate that TM effector proteins directly sense nucleotide second messenger signaling and subsequently initiate a cell death cascade that results in bacterial membrane disruption and restriction of phage propagation. TM effectors are the most prevalent form of CD-NTase-associated effector proteins (Burroughs et al., 2015; Millman et al., 2020), revealing direct membrane targeting as a critical feature of CBASS antiviral defense.

Analysis of the CBASS protein Cap15 explains a mechanism for how TM effectors disrupt membrane integrity and terminate phage replication. Cap15 activation specifically triggers collapse of the bacterial inner membrane and subsequent cytoplasmic condensation. Disruption of the inner membrane causes shrinking away from the outer membrane and cell wall and eventually results in complete membrane rupture and cell death (Figure 5). Microscopy images of bacteria succumbing to Cap15-induced death reveal a phenotype similar to *E. coli* cells dying from genetic disruption of lipid homeostasis (Sutterlin et al., 2016). While Cap15 is the most common TM effector, our results identify several additional families of CBASS TM effectors, including Cap14 (TM-SAVED) and Cap16 (TM-NUDIX), that respond to antiviral nucleotide second messenger signaling and similarly induce cell death (Figure 1E). We show that Cap14 also specifically triggers inner-membrane rupture (Figures S5G–S5K), demonstrating that direct targeting of membrane integrity is a shared feature among diverse CBASS operons. Interestingly, Cap14- and Cap15-mediated death exhibit altered dynamics and collapsed membrane morphologies, suggesting that while the overall mechanism of inner-membrane disruption is conserved, CBASS TM effectors may use distinct molecular mechanisms to induce cell death.

Our structural characterization of Cap15 additionally explains a mechanism for how TM effectors sense and respond to antiviral nucleotide second messenger signals. Crystal structures of *Ya*Cap15 reveal a compact β-barrel domain with a hydrophobic lower core that enables formation of a central ligand-binding pocket for specific nucleotide recognition (Figures 2 and 3). The minimized architecture of *Ya*Cap15 mirrors the structural principles used for rational design of small-molecule sensors (Dou et al., 2018), revealing a remarkable convergence between synthetic protein design and natural evolution of a nucleotide-sensing domain. The Cap15 β-barrel domain occurs in ~25% of the TM effectors in CBASS operons, representing discovery of >600 protein sensors capable of sensitively responding to diverse cyclic oligonucleotide signals. These β-barrel nucleotide-binding domains expand the list of structurally defined nucleotide second messenger receptors in bacterial and metazoan antiviral immunity including CARF/SAVED-family proteins and NucC receptors in bacteria (Jia et al., 2019; Lau et al., 2020; Lowey et al., 2020; Niewoehner and Jinek, 2016), STING-family receptors in bacteria and animal cells (Morehouse et al., 2020; Ouyang et al., 2012; Yin et al., 2012), and RECON-like receptors in animals (McFarland et al., 2017). We further show that like soluble CBASS effectors, Cap15 is activated through protein oligomerization. The organization of Cap15 as a discrete nucleotide-binding domain fused to cell-death-inducing TM segments further supports that CBASS effectors use a modular architecture to couple nucleotide second messenger recognition with diverse downstream effector functions (Lowey et al., 2020). The modular organization of CBASS effectors facilitates rapid diversification of new effector functions to combat phage replication and likely enables CD-NTase and STING acquisition during evolution of metazoan cGAS-STING signaling from CBASS precursor components (Morehouse et al., 2020; Whiteley et al., 2019).

Given membrane-targeting effectors are predominant in CBASS defense operons, inner-membrane disruption likely provides a key evolutionary advantage in phage defense. Sequence analysis of CBASS operons supports frequent horizontal transfer

(F) Time-lapse images of *E. coli* expressing WT *Vc*DncV and *Ea*Cap15 in the presence of the live-dead stain TO-PRO-3 and periplasmic mCherry. After inner-membrane collapse, the cells return to phase dark, are permeable to TO-PRO-3, and leak mCherry throughout the cell, confirming inner-membrane rupture and cell death.

(G) Schematic representation of membrane morphology observed upon Cap15 activation, with membranes shown in black, peptidoglycan shown in gray, and periplasm shown in red.

(H) Transmission electron microscopy of *E. coli* dying after *Ea*Cap15 activation, highlighting collapse of the inner membrane from the cell wall.

Light microscopy data are representative of at least three independent experiments. See also Figures S4 and S5.

and exchange between divergent bacterial species (Burroughs et al., 2015; Millman et al., 2020). CBASS effector proteins mediating cell death must, therefore, target ubiquitous host components to remain functional when shared between gram-negative and gram-positive bacteria. In line with this prediction, our results support that the vast majority of CBASS effectors target the conserved inner membrane (TM effectors and phospholipases) or dsDNA (DNA endonucleases). Targeting the host inner membrane to control abortive infection may be particularly advantageous, as successful phage replication requires maintenance of normal host membrane physiology until precisely timed activation of lytic machinery facilitates virion release (Cahill and Young, 2019). Interestingly, phages in the order *Caudovirales*, including all dsDNA phages demonstrated here to be susceptible to CBASS TM effectors, use perturbations of the membrane to trigger the inner-membrane proteins holin or pinholin to initiate cell lysis and virion release (Cahill and Young, 2019). The ability of CBASS TM effectors to prematurely disrupt membrane integrity likely short-circuits this process and enhances antiviral defense. Phages have evolved elaborate modification systems to protect viral DNA from recognition and cleavage (Stern and Sorek, 2011), and it will be interesting to uncover if mechanisms exist that allow escape from direct host membrane disruption.

Limitations of the study

Here, we report the structure of the CBASS Cap15 ligand-binding domain and present mutational analysis of a putative ligand-binding pocket. We also show that ligand binding induces oligomerization of Cap15, consistent with the activation mechanism observed for other CBASS effectors (Lau et al., 2020; Lowey et al., 2020; Morehouse et al., 2020). Further structural studies of full-length Cap15 in an activated state will be required to define how ligand binding induces oligomerization and how CBASS TM effector clustering results in membrane disruption. An additional limitation of our study is that the CBASS TM effector experiments analyze death only in the gram-negative host *E. coli*. Cap15 and CBASS TM effectors are broadly distributed among bacteria phyla, and it will be intriguing to compare how the mechanism of cell death and antiphage defense may differ in gram-positive hosts.

STAR★METHODS

Detailed methods are provided in the online version of this paper and include the following:

- KEY RESOURCES TABLE
- RESOURCE AVAILABILITY
  - Lead contact
  - Materials availability
  - Data and code availability
- EXPERIMENTAL MODEL AND SUBJECT DETAILS
  - *Escherichia coli* strains and phages
- METHOD DETAILS
  - Protein expression and purification
  - Effector-induced killing assay
  - Quantification of cell death by flow cytometry
  - Bioinformatics analyses
  - Crystallization and structure determination
  - CD-NTase product thin layer chromatography
  - YaCdnE product purification and analysis by HPLC
  - Mass spectrometry
  - Electrophoretic mobility shift assay
  - Thermal shift assay
  - SEC-MALS
  - Plasmid and strain construction
  - Plaque assays
  - Microscopy
  - Transmission electron microscopy
- QUANTIFICATION AND STATISTICAL ANALYSIS

SUPPLEMENTAL INFORMATION

Supplemental information can be found online at https://doi.org/10.1016/j.molcel.2021.10.020.

ACKNOWLEDGMENTS

The authors are grateful to Tobias Herrmann, Thomas Bernhardt, Stephen Harrison, Amy S.Y. Lee, and members of the Kranzusch lab for helpful comments and discussion; Harvard University's Center for Macromolecular Interactions; Paula Montero Llopis and the Microscopy Resources on the North Quad (MicRoN) core at Harvard Medical School; and Morten Danielsen and Daniel Malhiero for assistance with mass spectrometry. Electron microscopy imaging was performed in the HMS Electron Microscopy Facility. The work was funded by the Pew Biomedical Scholars Program (P.J.K.), Burroughs Wellcome Fund PATH award (P.J.K.), Mark Foundation For Cancer Research (P.J.K.), Mathers Foundation (P.J.K.), Parker Institute for Cancer Immunotherapy (P.J.K.), the European Research Council (grant ERC-CoG 681203 to R.S.), the Ernest and Bonnie Beutler Research Program of Excellence in Genomic Medicine (R.S.), the Minerva Foundation (R.S.), and the Knell Family Center for Microbiology (R.S.). B.D.-L. is supported as a Herchel Smith Graduate Research Fellow.

AUTHOR CONTRIBUTIONS

Experiments were designed by B.D.-L. and P.J.K. Crystallography and biochemical experiments were performed by B.D.-L. and N.K.M.-B. Bacterial toxicity experiments and microscopy were performed by B.D.-L. Phage challenge assays were performed by N.T. and R.S. The manuscript was written by B.D.-L. and P.J.K., and all authors contributed to editing the manuscript and support the conclusions.

DECLARATION OF INTERESTS

R.S. is a scientific cofounder and advisor of BiomX, Pantheon Bioscience, and Ecophage.

Received: May 31, 2021
Revised: August 31, 2021
Accepted: October 20, 2021
Published: November 15, 2021

REFERENCES

Adams, P.D., Afonine, P.V., Bunkóczi, G., Chen, V.B., Davis, I.W., Echols, N., Headd, J.J., Hung, L.W., Kapral, G.J., Grosse-Kunstleve, R.W., et al. (2010). PHENIX: a comprehensive Python-based system for macromolecular structure solution. Acta Crystallogr. D Biol. Crystallogr. *66*, 213–221.

Bernheim, A., Millman, A., Ofir, G., Meitav, G., Avraham, C., Shomar, H., Rosenberg, M.M., Tal, N., Melamed, S., Amitai, G., and Sorek, R. (2021). Prokaryotic viperins produce diverse antiviral molecules. Nature *589*, 120–124.

Burroughs, A.M., Zhang, D., Schäffer, D.E., Iyer, L.M., and Aravind, L. (2015). Comparative genomic analyses reveal a vast, novel network of nucleotide-centric systems in biological conflicts, immunity and signaling. Nucleic Acids Res. *43*, 10633–10654.

Cahill, J., and Young, R. (2019). Phage Lysis: Multiple Genes for Multiple Barriers. Adv. Virus Res. *103*, 33–70.

Chen, V.B., Arendall, W.B., 3rd, Headd, J.J., Keedy, D.A., Immormino, R.M., Kapral, G.J., Murray, L.W., Richardson, J.S., and Richardson, D.C. (2010). MolProbity: all-atom structure validation for macromolecular crystallography. Acta Crystallogr. D Biol. Crystallogr. *66*, 12–21.

Cohen, D., Melamed, S., Millman, A., Shulman, G., Oppenheimer-Shaanan, Y., Kacen, A., Doron, S., Amitai, G., and Sorek, R. (2019). Cyclic GMP-AMP signalling protects bacteria against viral infection. Nature *574*, 691–695.

Dal Peraro, M., and van der Goot, F.G. (2016). Pore-forming toxins: ancient, but never really out of fashion. Nat. Rev. Microbiol. *14*, 77–92.

Dewey, J.S., Savva, C.G., White, R.L., Vitha, S., Holzenburg, A., and Young, R. (2010). Micron-scale holes terminate the phage infection cycle. Proc. Natl. Acad. Sci. USA *107*, 2219–2223.

Dou, J., Vorobieva, A.A., Sheffler, W., Doyle, L.A., Park, H., Bick, M.J., Mao, B., Foight, G.W., Lee, M.Y., Gagnon, L.A., et al. (2018). De novo design of a fluorescence-activating β-barrel. Nature *561*, 485–491.

Emsley, P., and Cowtan, K. (2004). Coot: model-building tools for molecular graphics. Acta Crystallogr. D Biol. Crystallogr. *60*, 2126–2132.

Gabler, F., Nam, S.Z., Till, S., Mirdita, M., Steinegger, M., Söding, J., Lupas, A.N., and Alva, V. (2020). Protein Sequence Analysis Using the MPI Bioinformatics Toolkit. Curr. Protoc. Bioinformatics *72*, e108.

Govande, A.A., Duncan-Lowey, B., Eaglesham, J.B., Whiteley, A.T., and Kranzusch, P.J. (2021). Molecular basis of CD-NTase nucleotide selection in CBASS anti-phage defense. Cell Rep. *35*, 109206.

Hsiao, J.J., Potter, O.G., Chu, T.W., and Yin, H. (2018). Improved LC/MS Methods for the Analysis of Metal-Sensitive Analytes Using Medronic Acid as a Mobile Phase Additive. Anal. Chem. *90*, 9457–9464.

Jia, N., Jones, R., Yang, G., Ouerfelli, O., and Patel, D.J. (2019). CRISPR-Cas III-A Csm6 CARF Domain Is a Ring Nuclease Triggering Stepwise cA_4 Cleavage with ApA>p Formation Terminating RNase Activity. Mol. Cell *75*, 944–956.e6.

Jumper, J., Evans, R., Pritzel, A., Green, T., Figurnov, M., Ronneberger, O., Tunyasuvunakool, K., Bates, R., Žídek, A., Potapenko, A., et al. (2021). Highly accurate protein structure prediction with AlphaFold. Nature *596*, 583–589.

Kabsch, W. (2010). Xds. Acta Crystallogr. D Biol. Crystallogr. *66*, 125–132.

Karplus, P.A., and Diederichs, K. (2012). Linking crystallographic model and data quality. Science *336*, 1030–1033.

Kawato, T., Mizohata, E., Shimizu, Y., Meshizuka, T., Yamamoto, T., Takasu, N., Matsuoka, M., Matsumura, H., Kodama, T., Kanai, M., et al. (2015). Structure-based design of a streptavidin mutant specific for an artificial biotin analogue. J. Biochem. *157*, 467–475.

Krogh, A., Larsson, B., von Heijne, G., and Sonnhammer, E.L. (2001). Predicting transmembrane protein topology with a hidden Markov model: application to complete genomes. J. Mol. Biol. *305*, 567–580.

Lau, R.K., Ye, Q., Birkholz, E.A., Berg, K.R., Patel, L., Mathews, I.T., Watrous, J.D., Ego, K., Whiteley, A.T., Lowey, B., et al. (2020). Structure and Mechanism of a Cyclic Trinucleotide-Activated Bacterial Endonuclease Mediating Bacteriophage Immunity. Mol. Cell *77*, 723–733.e6.

Liebschner, D., Afonine, P.V., Baker, M.L., Bunkóczi, G., Chen, V.B., Croll, T.I., Hintze, B., Hung, L.W., Jain, S., McCoy, A.J., et al. (2019). Macromolecular structure determination using X-rays, neutrons and electrons: recent developments in Phenix. Acta Crystallogr. D Struct. Biol. *75*, 861–877.

Lopatina, A., Tal, N., and Sorek, R. (2020). Abortive Infection: Bacterial Suicide as an Antiviral Immune Strategy. Annu. Rev. Virol. *7*, 371–384.

Lowey, B., Whiteley, A.T., Keszei, A.F.A., Morehouse, B.R., Mathews, I.T., Antine, S.P., Cabrera, V.J., Kashin, D., Niemann, P., Jain, M., et al. (2020). CBASS Immunity Uses CARF-Related Effectors to Sense 3′-5′- and 2′-5′-Linked Cyclic Oligonucleotide Signals and Protect Bacteria from Phage Infection. Cell *182*, 38–49.e17.

Mazzocco, A., Waddell, T.E., Lingohr, E., and Johnson, R.P. (2009). Enumeration of bacteriophages using the small drop plaque assay system. Methods Mol. Biol. *501*, 81–85.

McFarland, A.P., Luo, S., Ahmed-Qadri, F., Zuck, M., Thayer, E.F., Goo, Y.A., Hybiske, K., Tong, L., and Woodward, J.J. (2017). Sensing of Bacterial Cyclic Dinucleotides by the Oxidoreductase RECON Promotes NF-κB Activation and Shapes a Proinflammatory Antibacterial State. Immunity *46*, 433–445.

Millman, A., Melamed, S., Amitai, G., and Sorek, R. (2020). Diversity and classification of cyclic-oligonucleotide-based anti-phage signalling systems. Nat. Microbiol. *5*, 1608–1615.

Morehouse, B.R., Govande, A.A., Millman, A., Keszei, A.F.A., Lowey, B., Ofir, G., Shao, S., Sorek, R., and Kranzusch, P.J. (2020). STING cyclic dinucleotide sensing originated in bacteria. Nature *586*, 429–433.

Mueller, M., Grauschopf, U., Maier, T., Glockshuber, R., and Ban, N. (2009). The structure of a cytolytic α-helical toxin pore reveals its assembly mechanism. Nature *459*, 726–730.

Niewoehner, O., and Jinek, M. (2016). Structural basis for the endoribonuclease activity of the type III-A CRISPR-associated protein Csm6. RNA *22*, 318–329.

Ouyang, S., Song, X., Wang, Y., Ru, H., Shaw, N., Jiang, Y., Niu, F., Zhu, Y., Qiu, W., Parvatiyar, K., et al. (2012). Structural analysis of the STING adaptor protein reveals a hydrophobic dimer interface and mode of cyclic di-GMP binding. Immunity *36*, 1073–1086.

Pang, T., Fleming, T.C., Pogliano, K., and Young, R. (2013). Visualization of pinholin lesions in vivo. Proc. Natl. Acad. Sci. USA *110*, E2054–E2063.

Severin, G.B., Ramliden, M.S., Hawver, L.A., Wang, K., Pell, M.E., Kieninger, A.K., Khataokar, A., O'Hara, B.J., Behrmann, L.V., Neiditch, M.B., et al. (2018). Direct activation of a phospholipase by cyclic GMP-AMP in El Tor *Vibrio cholerae*. Proc. Natl. Acad. Sci. USA *115*, E6048–E6055.

Sonnhammer, E.L., Eddy, S.R., and Durbin, R. (1997). Pfam: a comprehensive database of protein domain families based on seed alignments. Proteins *28*, 405–420.

Steinegger, M., and Söding, J. (2017). MMseqs2 enables sensitive protein sequence searching for the analysis of massive data sets. Nat. Biotechnol. *35*, 1026–1028.

Stern, A., and Sorek, R. (2011). The phage-host arms race: shaping the evolution of microbes. BioEssays *33*, 43–51.

Sutterlin, H.A., Shi, H., May, K.L., Miguel, A., Khare, S., Huang, K.C., and Silhavy, T.J. (2016). Disruption of lipid homeostasis in the Gram-negative cell envelope activates a novel cell death pathway. Proc. Natl. Acad. Sci. USA *113*, E1565–E1574.

Tanaka, K., Caaveiro, J.M., Morante, K., González-Mañas, J.M., and Tsumoto, K. (2015). Structural basis for self-assembly of a cytolytic pore lined by protein and lipid. Nat. Commun. *6*, 6337.

Uehara, T., Parzych, K.R., Dinh, T., and Bernhardt, T.G. (2010). Daughter cell separation is controlled by cytokinetic ring-activated cell wall hydrolysis. EMBO J. *29*, 1412–1422.

Wang, X., and Montero Llopis, P. (2016). Visualizing Bacillus subtilis During Vegetative Growth and Spore Formation. Methods Mol. Biol. *1431*, 275–287.

Weiss, M.S. (2001). Global indicators of X-ray data quality. J. Appl. Cryst. *34*, 130–135.

Whiteley, A.T., Eaglesham, J.B., de Oliveira Mann, C.C., Morehouse, B.R., Lowey, B., Nieminen, E.A., Danilchanka, O., King, D.S., Lee, A.S.Y., Mekalanos, J.J., and Kranzusch, P.J. (2019). Bacterial cGAS-like enzymes synthesize diverse nucleotide signals. Nature *567*, 194–199.

Ye, Q., Lau, R.K., Mathews, I.T., Birkholz, E.A., Watrous, J.D., Azimi, C.S., Pogliano, J., Jain, M., and Corbett, K.D. (2020). HORMA Domain Proteins and a Trip13-like ATPase Regulate Bacterial cGAS-like Enzymes to Mediate Bacteriophage Immunity. Mol. Cell *77*, 709–722.e7.

Yin, Q., Tian, Y., Kabaleeswaran, V., Jiang, X., Tu, D., Eck, M.J., Chen, Z.J., and Wu, H. (2012). Cyclic di-GMP sensing via the innate immune signaling protein STING. Mol. Cell *46*, 735–745.

Young, I., Wang, I., and Roof, W.D. (2000). Phages will out: strategies of host cell lysis. Trends Microbiol. *8*, 120–128.

Zhou, W., Whiteley, A.T., de Oliveira Mann, C.C., Morehouse, B.R., Nowak, R.P., Fischer, E.S., Gray, N.S., Mekalanos, J.J., and Kranzusch, P.J. (2018). Structure of the Human cGAS-DNA Complex Reveals Enhanced Control of Immune Surveillance. Cell *174*, 300–311.e11.

Zimmermann, L., Stephens, A., Nam, S.Z., Rau, D., Kübler, J., Lozajic, M., Gabler, F., Söding, J., Lupas, A.N., and Alva, V. (2018). A Completely Reimplemented MPI Bioinformatics Toolkit with a New HHpred Server at its Core. J. Mol. Biol. *430*, 2237–2243.

Please cite this article in press as: Duncan-Lowey et al., Effector-mediated membrane disruption controls cell death in CBASS antiphage defense, Molecular Cell (2021), https://doi.org/10.1016/j.molcel.2021.10.020

STAR★METHODS

KEY RESOURCES TABLE

REAGENT or RESOURCE	SOURCE	IDENTIFIER
Bacterial and virus strains		
E. coli BL21-DE3 RIL	Agilent	230245
E. coli BL21-DE3	New England Biolabs	C2527I
Chemicals, peptides, and recombinant proteins		
Ni-NTA Agarose	QIAGEN	30250
HiTrap Q HP Column	GE Healthcare	17115401
HiLoad 16/600 Superdex 75 PG	GE Healthcare	28989333
Zorbax Bonus-RP	Agilent	863668-901
SRT SEC-300	Sepax	215300-7830
[α-^{32}P] ATP	Perkin Elmer	BLU003H250UC
[α-^{32}P] GTP	Perkin Elmer	BLU006H250UC
[α-^{32}P] UTP	Perkin Elmer	BLU007H250UC
[α-^{32}P] CTP	Perkin Elmer	BLU008H250UC
PEI-Cellulose F TLC plate	EMD Biosciences	EM1.05579.0001
Alkaline Phosphatase, Calf Intestinal (CIP)	New England Biolabs	M0290S
NTPs	New England Biolabs	N0450S
SYPRO Orange	ThermoFisher	S6650
HEPES	VWR	97061-824
PEG-200	Sigma-Aldrich	P3015-500G
ADA	Sigma-Aldrich	A9883-25G
Tris[-2carboxyethyl] phosphine hydrochloride (TCEP)	GoldBio	TCEP50
3′3′-cUU	Biolog Life Science Institute GmbH & Co.	C 256
3′3′-cUA	Biolog Life Science Institute GmbH & Co.	C 357
3′3′-cUC	Biolog Life Science Institute GmbH & Co.	C 375
3′3′-cUG	Biolog Life Science Institute GmbH & Co.	C 371
3′3′-c-di-AMP	Biolog Life Science Institute GmbH & Co.	C 088
Deposited data		
*Ya*Cap15 (1.9 Å)	This paper	PDB: 7N34
*Ya*Cap15 (2.6 Å)	This paper	PDB: 7N35
Raw data	This paper	https://dx.doi.org/10.17632/zdrzpgyw24.1
Software and algorithms		
Phenix 1.13-2998	Adams et al., 2010	https://phenix-online.org/
Coot 0.8.9	Emsley and Cowtan, 2004	https://www2.mrc-lmb.cam.ac.uk/personal/pemsley/coot/
Pymol v1.7.4.4	Schrödinger, LLC	https://pymol.org/2/
Prism 7.0d	GraphPad software	https://www.graphpad.com/scientific-software/prism/

RESOURCE AVAILABILITY

Lead contact

Further information and requests for resources and reagents should be directed to and will be fulfilled by the Lead Contact, Philip J. Kranzusch (philip_kranzusch@dfci.harvard.edu).

Please cite this article in press as: Duncan-Lowey et al., Effector-mediated membrane disruption controls cell death in CBASS antiphage defense, Molecular Cell (2021), https://doi.org/10.1016/j.molcel.2021.10.020

Materials availability

This study did not generate new unique reagents.

Data and code availability

- Coordinates of the *Ya*Cap15 structures have been deposited in the RCSB Protein Data Bank under the following accession numbers: 7N34, 7N35.
- This paper does not report original code.
- Any additional information required to reanalyze the data reported in this paper is available from the lead contact upon request.

EXPERIMENTAL MODEL AND SUBJECT DETAILS

Escherichia coli strains and phages

BL21-RIL *E. coli* (Agilent) and BL21(DE3) *E. coli* (NEB) were transformed and plated on MDG plates (0.5% glucose, 25 mM Na_2HPO_4, 25 mM KH_2PO_4, 50 mM NH_4Cl, 5 mM Na_2SO_4, 2 mM MgSO4, 0.25% aspartic acid, 100 mg mL^{-1} ampicillin, 34 mg mL^{-1} chloramphenicol, and trace metals), then colonies were used to inoculate overnight MDG cultures. Overnight MDG cultures were used to inoculate M9ZB cultures (0.5% glycerol, 1% Cas-amino Acids, 47.8 mM Na_2HPO_4, 22 mM KH_2PO_4, 18.7 mM NH_4Cl, 85.6 mM NaCl, 2 mM $MgSO_4$, 100 mg mL^{-1} ampicillin, 34 mg mL^{-1} chloramphenicol, and trace metals), which were grown in each experiment as described below.

For phage challenge studies, *E. coli* strain MG1655 (ATCC 47076) was grown in MMB (LB media supplemented with 0.1 mM $MnCl_2$, 5 mM $MgCl_2$, with or without 0.5% agar) at room temperature. Whenever applicable, media were supplemented with ampicillin (100 μg mL^{-1}), to ensure the maintenance of plasmids. Infection was performed in MMB media at room temperature. Phages used in this study are listed in Table S1.

METHOD DETAILS

Protein expression and purification

Recombinant TM effector proteins, Cap15 effector mutants, and CD-NTase enzymes were purified as previously described (Lowey et al., 2020; Zhou et al., 2018). Briefly, CD-NTases and effectors were cloned into an N-terminal 6 × His-SUMO2-tagged pET vector and transformed into BL21-RIL *E. coli* (Agilent). Large scale cultures (2–4 l) were grown for ~5 h at 37°C, then induced with IPTG overnight at 16°C. Bacterial pellets were resuspended and sonicated in lysis buffer (20 mM HEPES-KOH pH 7.5, 400 mM NaCl, 30 mM imidazole, 10% glycerol and 1 mM DTT) and purified using Ni-NTA resin (QIAGEN). Ni-NTA resin was washed with lysis buffer supplemented to 1 M NaCl and eluted with lysis buffer supplemented to 300 mM imidazole. The Ni-NTA elution fraction was dialyzed into 20 mM HEPES-KOH pH 7.5, 250 mM KCl, 1 mM DTT overnight while removing the SUMO2 tag with recombinant human SENP2 protease (D364–L589, M497A). Proteins were concentrated using a 10K-cutoff concentrator (Millipore) and purified by size exclusion chromatography on a 16/600 Superdex 75 column. Proteins were concentrated to > 30 mg mL^{-1}, flash frozen with liquid nitrogen, and stored at −80°C.

Effector-induced killing assay

Plasmids expressing wild-type or catalytically inactive *Vc*DncV (D131A, D133A) (pBAD33) and an effector protein (custom pET, see Table S1) were transformed into competent *Escherichia coli* BL21(DE3) (NEB) and plated onto plates with MDG media (0.5% glucose, 25 mM Na_2HPO_4, 25 mM KH_2PO_4, 50 mM NH_4Cl, 5 mM Na_2SO_4, 2 mM MgSO4, 0.25% aspartic acid, 100 mg mL^{-1} ampicillin, 34 mg mL^{-1} chloramphenicol, and trace metals). After overnight incubation, 5 mL MDG starter cultures were inoculated with 3 colonies each and grown overnight at 37°C with 230 RPM shaking. Cultures were diluted 1:50 into 5 mL M9ZB cultures (0.5% glycerol, 1% Cas-amino Acids, 47.8 mM Na_2HPO_4, 22 mM KH_2PO_4, 18.7 mM NH_4Cl, 85.6 mM NaCl, 2 mM $MgSO_4$, 100 mg mL^{-1} ampicillin, 34 mg mL^{-1} chloramphenicol, and trace metals) and grown for 3 h at 37°C with 230 RPM shaking. Cultures were then diluted 1:5 into fresh M9ZB media with a final concentration of 0.2% arabinose and 5 μM IPTG to induce protein expression; 200 μL of culture were added to 96-well plate and OD_{600} was recorded in technical triplicate over 300 min in a Synergy H1 plate reader (BioTek), while shaking at 37°C. Wells containing media alone were used for OD_{600} background subtraction. Each biological replicate was measured in technical triplicate. OD_{600} at 300 min (WT/mut *Vc*DncV) was calculated as the OD_{600} of cultures expressing WT *Vc*DncV and effector divided by the OD_{600} of cultures expressing catalytically inactive *Vc*DncV and effector. This value was then divided by same ratio calculated for cultures expressing WT or mut. *Vc*DncV and a GFP control in place of effector. This calculation is represented by one data point in Figure 1E; all cultures used within one calculation were grown concurrently.

Quantification of cell death by flow cytometry

E. coli expressing *Vc*DncV and effector proteins were grown as induced as described above in effector-induced killing assays. After cultures were grown with inducer for 2 h, bacteria were diluted into 1 × PBS with an approximate final dilution of 1:500 of cultures that had an OD_{600} of 1. The cell-impermeable nucleic acid dye, TO-PRO-3 iodide (ThermoFisher) was added to a final concentration of 500 nM. Cells were analyzed using an LSR-II Analyzer (BD Biosciences) with excitation with a 633 nm laser and 660/20 emission filter.

Please cite this article in press as: Duncan-Lowey et al., Effector-mediated membrane disruption controls cell death in CBASS antiphage defense, Molecular Cell (2021), https://doi.org/10.1016/j.molcel.2021.10.020

Cells expressing WT *Vc*DncV and no effector were used to define gates on single cells using side scatter area versus side scatter width, the to define gating for TO-PRO-3-negative live cells.

Bioinformatics analyses

Previously-identified CBASS effectors (Millman et al., 2020) were assigned to clusters with at least 20% identity over 60% of the sequence using MMseqs2 (Gabler et al., 2020; Steinegger and Söding, 2017; Zimmermann et al., 2018). Clusters were further grouped into families using Pfam to identify at least two sequences within the cluster with a Pfam assignment (Sonnhammer et al., 1997).

SAVED domains within Cap14 were modeled using AlphaFold2.0 (Jumper et al., 2021). The AlphaFold prediction for the domain previously annotated as SUa (Pfam PF18179) allowed for the identification of this family of proteins as containing SAVED domains.

Transmembrane domains were identified within experimentally determined structures where available (Mueller et al., 2009; Tanaka et al., 2015), and were otherwise predicted using TMHMM (Krogh et al., 2001). Where modeled transmembrane domains are displayed, they were modeled using AlphaFold2.0 (Jumper et al., 2021).

Crystallization and structure determination

Cap15 proteins were crystallized at 18°C using the hanging drop method. Concentrated protein stocks were thawed on ice and diluted in buffer (25 mM HEPES-KOH pH 7.5, 1 mM TCEP). Drops were set by mixing protein stock and reservoir solution in 2 μL drops over a 350 μL reservoir in 15-well Easy-Xtal trays (NeXtal). Each protein was crystallized as follows: *Ya*Cap15 W78–end C 1 2 1 crystal form, selenomethionine *Ya*Cpa15 W78–end was diluted to 10 mg mL^{-1} and mixed at a 1:1 ratio of protein:reservoir solution (40% PEG-200, 0.1 M ADA pH 5.8); *Ya*Cap15 W78–end P 6_1 crystal form, *Ya*Cap15 W78–end was diluted to 10 mg mL^{-1} and mixed at a 1:1 ratio of protein:reservoir solution (40% PEG-200, 0.1 M ADA pH 5.3). In each case, crystals were harvested directly from the mother liquor without additional cryoprotectant, and flash frozen in liquid nitrogen.

X-ray data were collected at the Northeastern Collaborative Access Team beamlines 24-ID-C (P30 GM124165), and used a Pilatus detector (S10RR029205), an Eiger detector (S10OD021527) and the Argonne National Laboratory Advanced Photon Source (DE-AC02-06CH11357). X-ray crystallography data were processed with XDS and AIMLESS (Kabsch, 2010) using the SSRL autoxds script (A. Gonzalez, Stanford SSRL). Experimental phase information for *Ya*Cap15 was determined using data collected from selenomethionine-substituted C 1 2 1 crystal form crystals. One site was identified with HySS and an initial map was produced using SOLVE/RESOLVE in Phenix (Liebschner et al., 2019). Model building was performed using Coot (Emsley and Cowtan, 2004), then refined in Phenix. Statistics were analyzed as described in Table 1 (Chen et al., 2010; Karplus and Diederichs, 2012; Weiss, 2001).

CD-NTase product thin layer chromatography

Purified *Ya*CdnE was mixed at a final concentration of 1 μM with 25 μM NTPs and trace α-^{32}P-NTP in 10 μL reactions with 50 mM KCl, 10 mM $MgCl_2$, 1 mM DTT, and 50 mM CAPSO pH 9.0. These reactions were incubated for 2 h at 37°C and then terminated by treatment with 1 μL of 5 units μL^{-1} Calf Intestinal Phosphatase (New England Biolabs) for 1 h at 37°C. 1 μL of each reaction was spotted on a PEI-cellulose thin layer chromatography (TLC) plate (Millipore) and developed in a 1.5 M KH_2PO_4 pH 3.8 buffer until the solvent front was ~1 cm from the top of plate. TLC plates were dried and the exposed to a phosphor screen followed by imaging with an Amersham Typhoon IP (Cytiva).

YaCdnE product purification and analysis by HPLC

Large scale *Ya*CdnE product synthesis was carried out in 20 mL reactions with 1 μM purified *Ya*CdnE and 250 μM ATP, CTP, GTP, and UTP in 1 × reaction buffer (50 mM KCl, 20 mM $MgCl_2$, 40 mM CAPSO pH 9.0, 1 mM TCEP), then incubated overnight at 37°C with gentle shaking. The reaction was then treated with 10 μL of 5 units μL^{-1} Calf Intestinal Phosphatase (New England Biolabs) at 37°C overnight before filtering through a 0.2 μm filter. The reaction was diluted to 12.5 mM KCl with water, then loaded onto a 5 mL HiTrap Q column (GE Healthcare) at 1 mL min^{-1} with a peristaltic pump and eluted on an AKTA FPLC (GE Healthcare) with a linear gradient of ammonium acetate from 0–2 M over 60 min. Fractions from the two major peaks were identified by absorbance at 254 nm.

Comparison of major peak products to cyclic dinucleotide standards (3′3′-c-di-UMP [Biolog C 256], 3′3′-cUMP–CMP [Biolog C 375], 3′3′-cUMP–AMP [Biolog C 357]) was carried out using a C18 column (Agilent Zorbax Bonus-RP 4.6 × 150 mm, 3.5-micron). The column was heated to 40°C and run at 1 mL min^{-1} with a mobile phase of 50 mM NaH_2PO_4 (pH 6.8 with NaOH) supplemented with 3% acetonitrile.

Mass spectrometry

*Ya*CdnE reactions containing 25 μM ATP, GTP, CTP, and UTP, 10 mM $MgCl_2$, 50 mM KCl, 50 mM CAPSO pH 9, 1 mM DTT, and 10 μM enzyme with a final volume of 200 μL. Reactions were incubated overnight and treated with 1 μL of 5 units μL^{-1} Calf Intestinal Phosphatase (New England Biolabs) for 1 h at 37°C. Sample analysis was carried out by MS-Omics as follows. Samples were diluted 1:3 in 10% ultra-pure water and 90% acetonitrile containing 10 mM ammonium acetate at pH 9 then filtered through a Costar Spin-X centrifuge tube filter 0.22 μm Nylon membrane. The analysis was carried out using a Thermo Scientific Vanquish LC coupled to Thermo Q Exactive HF MS. An electrospray ionization interface was used as ionization source. Analysis was performed in positive ionization mode. Peak integration was performing using Tracefinder 4.0 and the extracted data was used to create a calibration curve to quantify the samples The UPLC was modified from previously-reported protocols (Hsiao et al., 2018).

Please cite this article in press as: Duncan-Lowey et al., Effector-mediated membrane disruption controls cell death in CBASS antiphage defense, Molecular Cell (2021), https://doi.org/10.1016/j.molcel.2021.10.020

Electrophoretic mobility shift assay

Radiolabeled 3′3′-c-di-UMP, 3′3′-cUMP–AMP, and 3′3′-c-di-AMP were synthesized by combining 25 μM NTPs and trace α^{32}P-NTP with purified enzymes *Ya*CdnE (3′3′-c-di-UMP: UTP, α^{32}P-UTP), *Ec*CdnE (3′3′-cUMP–AMP: UTP, ATP, α^{32}P-UTP), and *V. cholerae* DncV (3′3′-c-di-AMP: ATP, α^{32}P-ATP) at a final protein concentration of 1 μM in a 20 μL reaction with 5 mM $MgCl_2$, 50 mM KCl, 50 mM Tris-HCl pH 9.0, 1 mM DTT. These reactions were incubated at 37°C for ~24 h and then terminated by treatment with 1 μL of 5 units μL^{-1} Calf Intestinal Phosphatase (New England Biolabs) for 1 h at 37°C followed by boiling at 95°C for 5 min. The radiolabeled cyclic dinucleotide reaction products were then added at a concentration of 10 nM to reactions containing the Cap15 nucleotide-binding domain or a no protein control in a buffer of 50 mM KCl, 5 mM $MgCl_2$, 50 mM Tris-HCl pH 7.5, and 1 mM TCEP. In wild-type *Ya*Cap15 nucleotide binding assays, binding was measured at protein concentrations ranging from 1 nM to 1 μM and in mutant *Ya*Cap15 nucleotide binding assays binding was measured at concentrations of 100 nM and 1 μM. Reactions were incubated for 10 min at 25°C then separated on a 6% nondenaturing polyacrylamide gel (7.2 cm, 29:1 acrylamide-bisacrylamide, 0.5 × TBE buffer) run at 100 V for 20 min in 0.5 × TBE buffer. The gel was immediately dried at 80°C for 1 h and then exposed to a phosphor screen followed by imaging with an Amersham Typhoon IP (Cytiva).

Signal intensity was calculated using ImageQuant TL 8.2 software (Cytiva). Background signal intensity, taken from the no protein control lane, was subtracted from each signal intensity reading. Percent ligand bound was calculated by dividing the signal intensity of the bound protein-ligand complex by the total signal intensity of both the unbound ligand and the protein-ligand complex. Where two bands are present in the bound complex, the intensity of both bands was combined to calculate the bound fraction.

Thermal shift assay

Purified *Ya*Cap15 W78–end β-barrel, WT or containing point mutations as indicated, was added at a final concentration of 10 μM with 100 μM synthetic nucleotide ligands (Biolog) and 2 × SYPRO Orange Dye in a buffer of 75 mM KCl, 20 mM HEPES-KOH pH 7.5. Samples were slowly heated from 25 to 95°C over the course of 2 h using a qPCR CFX96 thermocycler (Biorad) and fluorescence in the SYBR channel was measured every 0.5°C. The first derivative of each fluorescence curve was calculated, and the melting temperature was identified as the peak of each derivative curve.

SEC-MALS

*Ya*Cap15 W78–end samples were prepared by diluting in SEC-MALS running buffer (150 mM KCl, 20 mM HEPES-KOH pH 7.5, 1 mM TCEP) to 1.25 mg mL^{-1} and incubating on ice for 5 min, then separated on an SRT SEC-150 column (Sepax). *Ya*Cap15 89–end W120A constructs were buffer exchanged into SEC-MALS running buffer (150 mM KCl, 20 mM HEPES-KOH pH 7.5, 1 mM TCEP) using a Superdex 200 Increase 10/300 column (Cytvia), then diluted to 1.25 mg mL^{-1}, incubated on ice for 5 min, then separated on an SRT SEC-150 column or SRT SEC-300 column (Sepax). Protein concentration was calculated using refractive index on a Wyatt Optilab T-rex Refractive Index Detector assuming dn dc^{-1} of 0.185 and a molar mass was calculated using a Wyatt Dawn Heleos II Multi-Angle Light Scattering detector and ASTRA software.

Plasmid and strain construction

Yersinia aleksiciae and *Escherichia albertii* CBASS operons used in this study were synthesized by Genscript Corp. and cloned into the pBAD plasmid (Thermofisher, cat. #43001), as previously described (Bernheim et al., 2021). *Escherichia albertii* and *Yersinia aleksiciae* CBASS operon mutants were constructed by Genscript Corp or cloned using PCR fragments and Gibson assembly. All synthesized sequences are presented in Table S1. Plasmids were transformed into *E. coli* strain MG1655.

Plaque assays

Phages were propagated by picking a single phage plaque into a liquid culture of *E. coli* MG1655 grown at 37°C to OD_{600} of 0.3 in MMB medium until culture collapse. The culture was then centrifuged for 10 min at 4,000 × RPM and the supernatant was filtered through a 0.2 μm filter to remove remaining bacteria and bacterial debris. Lysate titer was determined using the small drop plaque assay method as previously described (Mazzocco et al., 2009).

Plaque assays were performed as previously described (Mazzocco et al., 2009). Bacteria (*E. coli* MG1655 with CBASS-expressing cells) or negative control (*E. coli* MG1655 with a pBAD-GFP vector) were grown overnight at 37°C. Then 300 μL of the bacterial culture was mixed with 30 mL melted MMB agar (LB media supplemented with 0.1 mM $MnCl_2$, 5 mM $MgCl_2$, 0.5% agar, and 0.2% arabinose) and left to dry for 1 h at room temperature. CBASS operons containing point mutations as indicated or Cap15 transmembrane regions were removed (*Ya*Cap15 W78–end).

10-fold serial dilutions in MMB were performed for each of the tested phages and 10 μL drops were spotted onto the bacterial layer. Plates were incubated overnight at room-temperature and plaque forming units (PFUs) were determined by counting the derived plaques after overnight incubation.

Microscopy

Plasmids expressing wild-type or catalytically inactive *Vc*DncV (D131A, D133A) (pBAD33) and an effector protein (custom pET) were transformed into competent *E. coli* BL21(DE3) (NEB) and plated onto plates with MDG media (0.5% glucose, 25 mM Na_2HPO_4, 25 mM KH_2PO_4, 50 mM NH_4Cl, 5 mM Na_2SO_4, 2 mM MgSO4, 0.25% aspartic acid, 100 μg mL^{-1} ampicillin, 34 μg mL^{-1} chloramphenicol, and

trace metals), then incubated overnight at 37°C. The next day, 5 mL MDG starter cultures were inoculated with 3 colonies each, then incubated overnight at 37°C with 230 RPM shaking. The next morning, overnight cultures were resuspended in 5 × volume M9ZB (0.5% glycerol, 1% Cas-amino Acids, 47.8 mM Na_2HPO_4, 22 mM KH_2PO_4, 18.7 mM NH_4Cl, 85.6 mM NaCl, 2 mM $MgSO_4$, 100 mg mL^{-1} ampicillin, 34 mg mL^{-1} chloramphenicol, and trace metals) and grown for 4 h at 37°C with 230 RPM shaking. Protein expression was then induced by resuspending cultures in 5 × volume of inducing media (M9ZB, 0.2% arabinose, 5 μM IPTG), and cultures were grown for 1.5 h at 37°C with 230 RPM shaking. Where indicated, the bacteria were additionally transformed with a plasmid expressing periplasmic mCherry as previously described (Uehara et al., 2010), and subjected to additional selection with 50 μg mL^{-1} spectinomycin.

Where indicated, 100 μL bacteria were stained with dyes by adding 1 μL of 100 × stocks: DAPI (ThermoFisher D1306) 0.2 mg mL^{-1}, FM4-64 (ThermoFisher T13320) 0.15 mg mL^{-1}, TO-PRO-3 iodide (ThermoFisher T3605) 50 μM. Bacteria were then plated on agarose pads (1.2% agarose, M9ZB, 0.4% arabinose, 10 μM IPTG, with additional FM4-64 15 μg mL^{-1} or 500 nM TO-PRO-3 iodide where indicated) and immediately covered with coverslip, as previously described (Wang and Montero Llopis, 2016). Slides were imaged between 2 and 4 h after initial induction; during time-lapse imaging, slides were maintained at 30°C. Images were acquired using a Nikon Ti microscope equipped with Plan Apo 100 × /1.40 Oil Ph3 DM objective and Andor Zyla 4.2 Plus sCMOS camera and Nikon Elements 4.30 acquisition software. Adobe Photoshop was used for brightness and contrast adjustments.

Transmission electron microscopy

E. coli expressing WT *Vc*DncV and *Ea*Cap15 were grown and induced as described for phase contrast microscopy. After 2.5 h, cells were pelleted and fixed in 2.5% paraformaldehyde, 5.0% glutaraldehyde, 0.06% picric acid in 0.2 M cacodylate buffer, followed by osmication and uranyl acetate staining, dehydration in graded alcohols and embedded in Taab 812 Resin (Marivac Ltd., Nova Scotia, Canada). Blocks/samples:80nm sections were cut with the Leica Ultracut S microtome, picked up on formvar-carbon coated slot Cu grids, stained with 0.2% Lead Citrate, and viewed and imaged under the Philips Tecnai BioTwin Spirit or JEOL 1200x Electron Microscope.

QUANTIFICATION AND STATISTICAL ANALYSIS

Statistical details for each experiment can be found in the figure legends and outlined in the corresponding methods details section. Data are plotted with error bars representing the standard deviation (SD).